Question of dynamic chirality in nuclei: The case of ^134 Pr

Tonev, D.; Angelis, G. de; Brant, Slobodan; Frauendorf, S.; Petkov, P.; Dewald, A.; Dönau, F.; Balabanski, D. L.; Zhong, Q.; Pejovic, P.; ...

Source / Izvornik: **Physical Review C - Nuclear Physics, 2007, 76**

Journal article, Published version
Rad u časopisu, Objavljena verzija rada (izdavačev PDF)

https://doi.org/10.1103/PhysRevC.76.044313

Permanent link / Trajna poveznica: https://urn.nsk.hr/urn:nbn:hr:217:511286

Question of dynamic chirality in nuclei: The case of ^{134}Pr

D. Tonev,[1,2] G. de Angelis,[1] S. Brant,[3] S. Frauendorf,[4,5] P. Petkov,[2] A. Dewald,[6] F. Dönau,[5] D. L. Balabanski,[2,7] Q. Zhong,[8] P. Pejovic,[6] D. Bazzacco,[9] P. Bednarczyk,[10,11] F. Camera,[12] D. Curien,[10] F. Della Vedova,[1] A. Fitzler,[6] A. Gadea,[1] G. Lo Bianco,[7] S. Lenzi,[9] S. Lunardi,[9] N. Marginean,[1] O. Möller,[6] D. R. Napoli,[1] R. Orlandi,[1] E. Sahin,[1] A. Saltarelli,[7] J. Valiente Dobon,[1] K. O. Zell,[6] Jing-ye Zhang,[13] and Y. H. Zhang[14]

[1]*INFN, Laboratori Nazionali di Legnaro, I-35020 Legnaro, Italy*
[2]*Institute for Nuclear Research and Nuclear Energy, Bulgarian Academy of Sciences, 1784 Sofia, Bulgaria*
[3]*Department of Physics, Faculty of Science, University of Zagreb, 10000 Zagreb, Croatia*
[4]*Department of Physics, University of Notre Dame, Notre Dame, Indiana 46556, USA*
[5]*Institute for Radiation Physics, Research Center Rossendorf, D-01314 Dresden, Germany*
[6]*Institut für Kernphysik der Universität zu Köln, D-50937 Köln, Germany*
[7]*Dipartimento di Fisica, Università di Camerino and INFN Perugia, I-62032 Camerino, Italy*
[8]*Department of Nuclear Physics, China Institute of Atomic Energy, Beijing 102413, People's Republic of China*
[9]*Dipartimento di Fisica dell' Università and INFN Sezione di Padova, I-35131 Padova, Italy*
[10]*Institut de Recherches Subatomiques, BP 28, F-67037 Strasbourg, France*
[11]*Institute of Nuclear Physics, PAN, 31-342 Kraków, Poland*
[12]*Dipartimento di Fisica dell' Università and INFN Sezione di Milano, I-20133 Milano, Italy*
[13]*Department of Physics and Astronomy, University of Tennessee, Knoxville, Tennessee 37996, USA*
[14]*Institute of Modern Physics, Chinese Academy of Sciences, Lanzhou 73000, People's Republic of China*

(Received 25 April 2007; published 17 October 2007)

Lifetimes of exited states in ^{134}Pr were measured by means of the recoil distance Doppler-shift and Doppler-shift attenuation techniques. The branching ratios and the electric or magnetic character of the transitions were also investigated. The experiments were performed at IReS, Strasbourg, using the EUROBALL IV spectrometer, in conjunction with the inner bismuth germanate ball and the Cologne coincidence plunger apparatus. Exited states in ^{134}Pr were populated in the fusion-evaporation reaction ^{119}Sn(^{19}F, $4n$)^{134}Pr. The possible chiral interpretation of twin bands was investigated in the two-quasiparticle triaxial rotor and interacting boson-fermion-fermion models. The analysis of the wave functions has shown that the possibility for the angular momenta of the proton, neutron, and core to find themselves in the favorable, almost orthogonal geometry, is present but is far from being dominant. The structure is characterized by large β and γ fluctuations. The existence of doublets of bands in ^{134}Pr can be attributed to weak chirality dominated by shape fluctuations.

DOI: 10.1103/PhysRevC.76.044313 PACS number(s): 21.10.Tg, 23.20.Lv, 27.60.+j

I. INTRODUCTION

Chirality has recently been proposed as a novel feature of rotating nuclei [1–3]. A spontaneous breaking of the chiral symmetry can take place for configurations where the angular momenta of the valence protons, valence neutrons, and the core are mutually perpendicular [4]. This can occur, for example, when the proton and neutron Fermi levels are located in the lower part of valence proton high-j (particle-like) and in the upper part of valence neutron high-j (hole-like) subshells and the core is triaxial. Under such conditions, the angular momenta of the valence particles are aligned along the short and long axes of the triaxial core, whereas the angular momentum of the rotational core is aligned along the intermediate axis. The resulting aplanar total angular momentum can be arranged into a left-handed or a right-handed systems, which differ by intrinsic chirality [2]. Because the chiral symmetry is dichotomic, its spontaneous breaking by the axial angular momentum vector leads to doublets of closely lying rotational bands of the same parity [1–3].

Pairs of bands possibly due to the breaking of the chiral symmetry have been found in a wide region of masses, namely $A \sim 105$ [5–7], $A \sim 130$ [8–12], $A \sim 190$ [13]. There is also a significant interest from theoretical point of view to investigate the chiral phenomenon [2,14–16]. In the present work we will concentrate our attention on the investigation of the nucleus ^{134}Pr shown to be a good candidate to express chirality [2,3]. The first example of two nearly degenerate bands with the same parity and spins has been reported for ^{134}Pr [17,18]. The two chiral candidate bands are displayed in Fig. 1. The degeneracy between levels of the same spin and parity is increasing with increasing spin and the bands cross above $I > 15\hbar$. In the context of chiral symmetry such a doublet of bands has been described within the framework of the particle-core coupling model [1,3] and the tilted-axis cranking model [2]. An alternative interpretation has been based on the interacting boson-fermion-fermion model (IBFFM) [19]. Here the energy degeneracy is also obtained but a different nature is attributed to the two bands. The yrast band is basically built on the ground-state configuration of the triaxial core, whereas the collective structure of the yrare band contains a large component of the γ band and, with increasing angular momentum, of higher-lying collective core structures.

To investigate nuclear chirality, next to establish the existence of almost degenerate rotational bands, it is necessary to

measure also other observables and compare them to the model predictions. Recently, our measured lifetimes [20] in the chiral candidates bands of ^{134}Pr showed that, contrary to the chiral predictions, the $B(E2)$ values of the transitions depopulating the analog states are different as well as that a $B(M1)$ staggering is not present. These experimental observables point to the fact that the limit of static chirality is not reached in ^{134}Pr and that the nucleus stays in a very soft vibrational regime. The experimentally determined transition matrix elements can be reproduced by taking into account the fluctuations of nuclear shape (IBFFM). This means that the chirality in ^{134}Pr, if it exists, has mainly a dynamical character. Thereby the coupling due to shape fluctuations seems to play a central role. It may also indicate that the coupling of the two quasiparticles to the shape degrees of freedom is the prominent mechanism. In a subsequent work [21], the observed properties of chiral candidates bands in ^{134}Pr are also critically analyzed and the authors put in question the presence of chirality in this nucleus. In this work we present in more detail the results of the experiments described in Ref. [20]: furthermore, the properties of the nearly degenerate pair bands of ^{134}Pr will be discussed and compared with theoretical models.

II. EXPERIMENT

To measure lifetimes of excited states in ^{134}Pr by using the recoil distance Doppler-shift (RDDS) and Doppler-shift attenuation (DSA) measurements, the fusion-evaporation reaction ^{119}Sn(^{19}F, 4n) at beam energies of 87 and 83 MeV, respectively, was used. The beam was delivered by the Vivitron accelerator at IReS in Strasbourg. For the RDDS measurement, the target consisted of 0.5 mg/cm^2 ^{119}Sn foil enriched to 89.8%. It was evaporated on a 1.8 mg/cm^2 ^{181}Ta foil facing the beam. A 6.0 mg/cm^2 gold foil was used to stop the recoils that were leaving the target with a mean velocity of 0.98(2)% of the velocity of light, c. For the DSAM measurement, the target consisted of 0.7 mg/cm^2 ^{119}Sn evaporated onto a 9.5 mg/cm^2 ^{181}Ta backing used to stop the recoils. The γ rays de-exciting the recoiling ^{134}Pr nuclei were detected using the EUROBALL IV [22] detector array composed of 26 clover and 15 cluster Ge detectors and an inner BGO (bismuth germanate) ball. The cluster and clover detectors of EUROBALL were grouped into 10 rings corresponding to approximately the same polar angle with respect to the beam axis, namely ring 1 ($\theta = 72.2^\circ$), ring 2 ($\theta = 80.9^\circ$), ring 3 ($\theta = 99.0^\circ$), ring 4 ($\theta = 107.4^\circ$), ring 5 ($\theta = 122.6^\circ$), ring 6 ($\theta = 130.4^\circ$), ring 7 ($\theta = 137.6^\circ$), ring 8 ($\theta = 147.5^\circ$), ring 9 ($\theta = 156.1^\circ$) and ring 10 ($\theta = 163.5^\circ$). For the present RDDS and DSAM measurements, the rings of main interest are those where appreciable Doppler shifts can be observed, i.e., rings 5, 6, 7, 8, 9, and 10. In the lifetime analysis, data only from one forward ring, namely ring number 1, were used. The trigger condition for data acquisition was set such that events were recorded when at least three γ rays in the Ge cluster or clover segments and three γ rays in the inner ball were in prompt coincidence. With such trigger conditions, the yield of ^{134}Pr was estimated to be 28% of the total cross section. Gain matching and efficiency calibration of the Ge detectors were performed using ^{133}Ba-, ^{152}Eu-, and ^{56}Co-radioactive sources. A standard add-back correction for Compton scattering was applied. For the RDDS measurement, data were taken at 20 target-to-stopper distances ranging from electrical contact to 2500 μm. Some of the investigated transitions have low energies, and because v/c is 0.98(2)%, the resulting Doppler shift is relatively small. For this reason, in the analysis, only detectors with good resolution were selected to obtain better line shapes. The good statistics for the low-lying states of ^{134}Pr allowed construction of γ-γ coincidence matrices in which the angular information is conserved on both axes. For the higher-lying states of ^{134}Pr, because of the weaker statistics, only matrices were constructed where one of the axes was associated with a specific detection angle, whereas on the other axis every detector (ring) firing in coincidence was allowed. For the RDDS case the normalization of the data taken at different target-to-stopper distances was performed using coincidence events corresponding to pairs of strong transitions. The level-scheme of ^{134}Pr obtained from the present data is reported in Fig. 1. Examples of spectra taken at different distances for two γ-ray transitions in ^{134}Pr are shown in Fig. 2.

III. DATA ANALYSIS

A. RDDS experiment

In the RDDS case, the lifetime determination is based on the precise knowledge of the areas of the shifted (S) peak, corresponding to an emission of a γ-ray transition depopulating the level of interest while the recoil nucleus is in flight in vacuum (or in slowdown, see below), and the area of the unshifted (U) peak, corresponding to an emission when the recoil is at rest in the stopper. In the RDDS measurements, the evolution of the intensity splitting between these two components that follows the change of the target-to-stopper distance is sensitive to the lifetime τ of the depopulating level. For the lifetime determination, we used the differential decay curve method (DDCM), proposed in Refs. [23,24]. According to this method, at each target-to-stopper distance x, the lifetime $\tau(x)$ of the level of interest is determined from quantities obtained directly from the measured data. The method can be applied for data analysis of singles as well as for coincidence measurements. In the case of coincidences, the lifetime can be obtained following the equation:

$$\tau(x) = \{B_S, A_U\}/(d\{B_S, A_S\}/dt). \quad (1)$$

In this equation, the quantities in brackets are the numbers of experimental coincident events detected for the shifted (S) and unshifted (U) part of the transitions involved in the analysis. The indices A and B denote decaying and directly feeding transitions and the gate is set on the shifted component of the directly feeding transition B.

Obviously the precision of the determination of the areas of the U and S peaks will set limitations on the precision of the investigated lifetime. The correct determination of the areas of shifted and unshifted peaks, however, depends on several factors, discussed in Ref. [25]. Here we mention only the

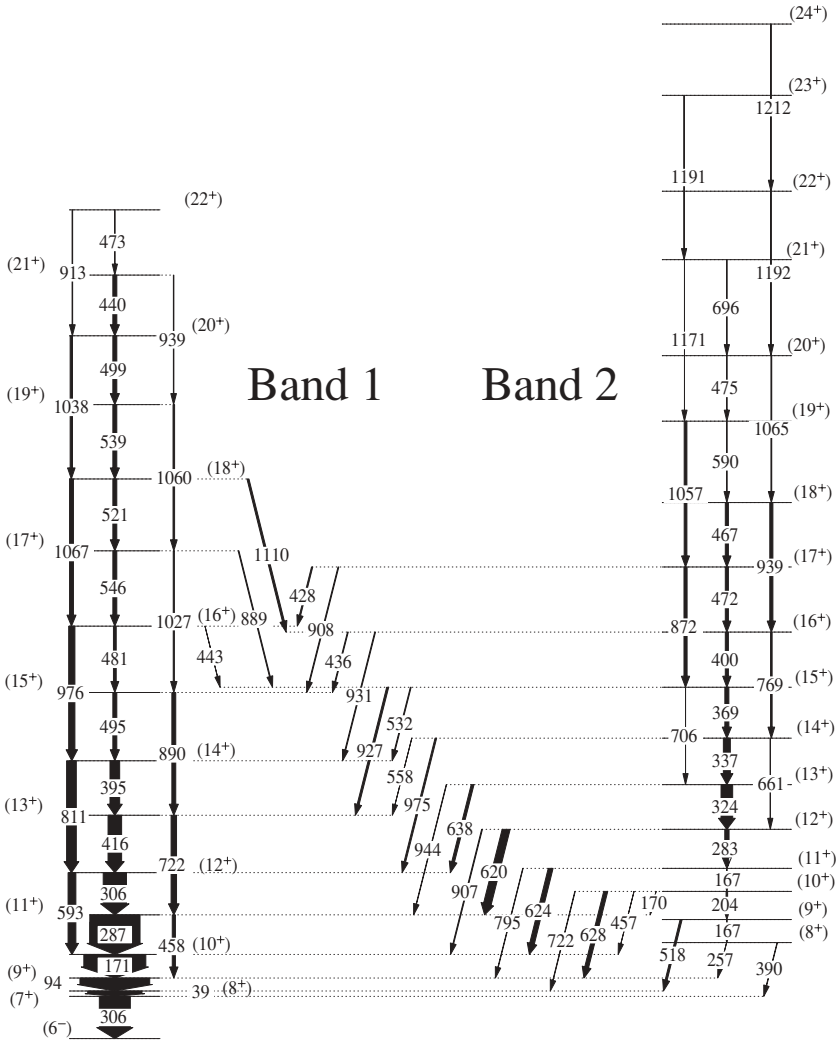

FIG. 1. Partial level scheme of ^{134}Pr from Ref. [26]. Two nearly degenerate positive-parity bands, candidates for chiral partner bands, are indicated as Band 1 and Band 2.

main points that are relevant for the present measurement. In our experiment the beam energy, chosen to ensure a maximal cross section for the nucleus of interest, was relatively small and leads to small recoil velocities [$v/c = 0.98(2)\%$]. In such a case the shifted and unshifted peaks are not well separated and we need to know exactly the line shapes of the two peaks to determine their areas. Whereas the shape of the U peak is described by the response function of the detector, the shape of the S peak depends also on the target thickness and stopping powers, the reaction used and the beam energy. All these factors practically determine the velocity distribution of the recoiling nuclei. Changing the distance between target and stopper leads to changes of the line shape of the shifted peak. The faster recoils reach the stopper earlier and they have higher possibility to emit γ rays at rest than the slower ones and in such a way faster recoils contribute more to the unshifted peak. For different target-to-stopper distances the fraction of these nuclei is different what leads to a modification of the line shape of the shifted peak.

One important effect that should be taken into account is that the recoils are not coming immediately at rest in the stopper; instead this occurs in a finite time interval. During this slowdown time they are moving and emitting γ rays. The detection of the emitted γ rays leads to the observation of a continuous Dopper-shift attenuated (DSA) spectrum. The effect is of importance when lifetimes comparable with or smaller than the slowdown time are determined, as it is for some lifetimes in our measurement [20]. Including the emission of γ rays during the slowdown in the stopper leads to a change of the standard Eq. (1), and its modified form [25] is of significant importance for the precise determination of short lifetimes:

$$\tau_a(x) = (\{B_{SF}, A_U\} + \{B_{SS}, A_U\}) \Big/ \big(d(\{B_{SF}, A_{SF}\} + \{B_{SF}, A_{SS}\} + \{B_{SS}, A_{SS}\})/dt_{f_f}\big). \quad (2)$$

In this equation, the index SF represents the emission in flight in vacuum, the additional index SS denotes the γ-ray emission occurring during the slowdown in the stopper, and the index U implies an emission from a fully stopped nucleus. The emission during the slowdown in the target can be neglected. In the denominator, the value of the derivative of the generalized "shifted" coincident area with respect to the end-flight time t_{f_f} is used. It should be mentioned that t_{f_f} denotes the time where the recoil reaches the stopper rather than the time spent during the flight in vacuum. Because the lifetimes τ are calculated at

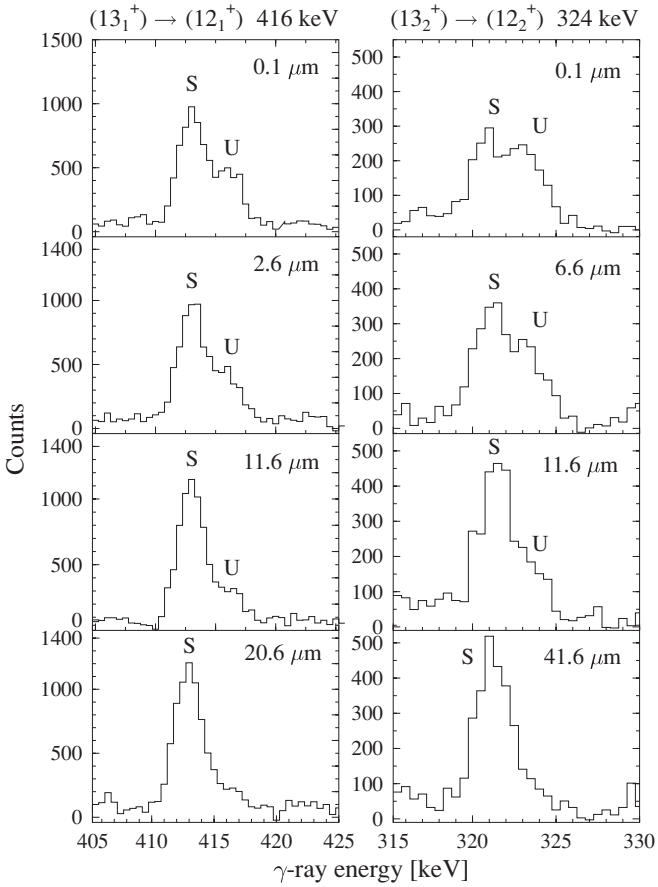

FIG. 2. Gated γ-ray spectra of ^{134}Pr taken at four different distances. Summed spectra from all detectors at a backward angle of 137.60° with respect to the beam axis are shown. On the left-hand side, both shifted and unshifted peaks of the $13_1^+ \rightarrow 12_1^+$ transition are presented. On the right-hand side, the shifted and unshifted peaks of the $13_2^+ \rightarrow 12_2^+$ transition are shown. At the distance 41.6 μm, the 323.6 keV transition ($13_1^+ \rightarrow 12_2^+$) is fully shifted, whereas the 416.2 keV transition ($13_1^+ \rightarrow 12_1^+$) has only a shifted component already at the distance of 20.6 μm.

each target-to-stopper distance x one obtains a function $\tau(x)$ or $\tau(\langle t_{f_f} \rangle)$, i.e., the so-called τ curve, expected to be a constant. Deviations from a constant behavior indicate the presence of systematic errors.

For the RDDS analysis we have used also a method that is a variant of the procedure [25] relevant for a case where a gating condition, e.g., a gate set on the full line shape of a transition, does not influence the timing information for the investigated level, i.e., in a singles-like mode. In this case the description of the line-shape is made as in Ref. [25], by correlating the time evolutions of the velocity distribution of the recoils and the population $n_a(t)$ of the de-exciting level a. The formalism concerning such an analysis in RDDS measurements is presented in details in Ref. [27]. To analyze the data, we used the procedures developed in Refs. [25,28]. Thereby, the background subtracted line shapes corresponding to the transition of interest at all distances and the shifted decay function $S_{af}(t)$ are fitted simultaneously. The function $S_{af}(t)$ is represented by continuously interconnected second-order polynomials over an arbitrarily chosen set of neighboring time intervals. The fitting problem is linear with respect to the polynomial parameters and the areas of the unshifted peak.

Finally, at each distance x or mean end-of-flight time $\langle t_{f_f} \rangle$ the lifetime of the state a, directly populated by transitions from level h and decaying by the transition to level f, is obtained by:

$$\tau(x) = \tau\left(\langle t_{f_f} \rangle\right) = \left[\tilde{R}_{af}(x) - b_{af} \sum_{h=1}^{N} (1 + \alpha_{ha}) \frac{I_{ha}^{\gamma} \tilde{S}_{af}(\infty)}{I_{af}^{\gamma} \tilde{S}_{ha}(\infty)} \tilde{R}_{ha}(x) \right] \Big/ \left\langle d\tilde{S}_{af}/dt \big|_{t=t_s} \right\rangle. \quad (3)$$

Here, $\tilde{R}$ denote the areas of the unshifted peaks, b_{af} is the branching ratio of the transition $a \rightarrow f$, α_{ha} are the internal conversion coefficients of the γ-ray transitions $h \rightarrow a$, I^{γ} are the relative intensities of the γ-ray transitions, and $\tilde{S}_{af}(\infty)$ are the values of the fitted shifted decay curves at large times (i.e., where they reach constant values). The γ-ray intensities have to be known independently indeed. The denominator represents the derivative $d\tilde{S}_{af}/dt$ averaged over the Monte Carlo (MC) histories used for the fits of the RDDS spectra and $\tilde{S}_{af}$.

To illustrate the application of the procedure, we show in Fig. 3 an example of the data for the 594 keV transition that depopulates the level $I^{\pi} = (12_1^+)$. On the left-hand side of the figure, line shapes measured at the indicated distances are displayed together with the fits. An inspection of Fig. 3 suggests that DSA contribution has to be taken into account for a precise analysis of the data.

For the description of the stopping process we used a modified version of the computer code DESASTOP [29,30] by G. Winter. This version allows for a numerical treatment of the electron stopping powers at relatively higher ion energies.

Finally, it should be mentioned that our code follows closely the MC calculation of the stopping process proposed by W. M. Currie [31]. The line shapes of the shifted peaks at large distances are satisfactorily reproduced using the simulated velocity distribution. Hence one can conclude that the stopping powers of the target material are correctly taken into account.

B. DSAM experiment

In the DSAM experiments the distance between target and stopper is fixed and it is zero. During the slowdown in the target and the stopper excited recoiling nuclei can emit γ rays, and the time period from the moment of the creation of the recoils until the moment they stop in the stopper determines the subpicosecond region of the applicability of this method. Experimentally, the method is realized by measuring the spectrum of γ rays by detectors positioned at a given direction of observation, e.g., at an angle θ with respect to the beam axis. The Doppler-shift formula $E'_{\gamma} = E_{\gamma_0}(1 + v_{\theta}/c)$ describes the relation between the precise registered energy E'_{γ}, the energy of the γ-ray emitted at rest E_{γ_0}, and the recoil velocity projection v_{θ} on this direction and thus correlates the decay and slowdown histories. The measured line shape is the result of the folding of the energy signal with the response function Φ of the detector, and it is described by the

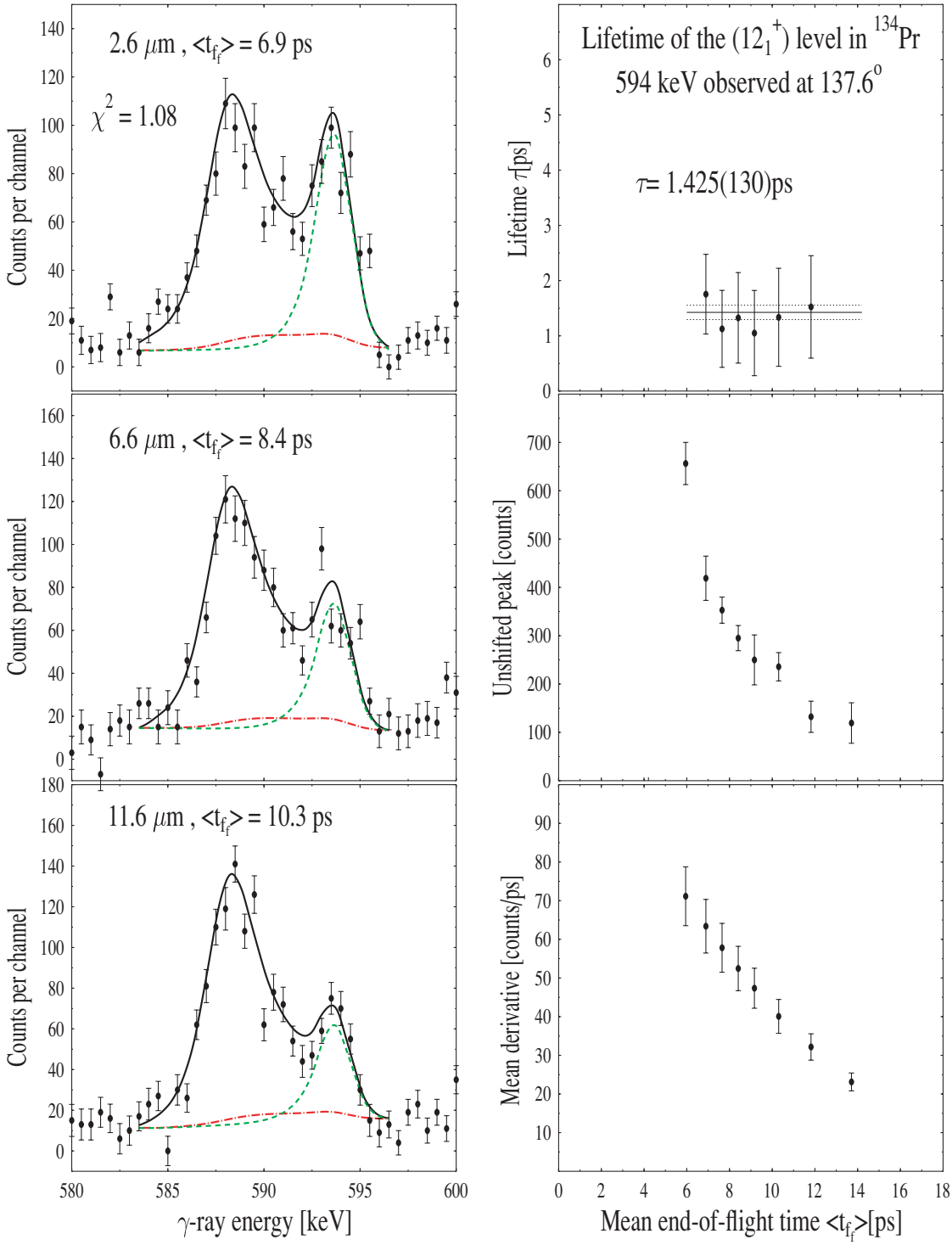

FIG. 3. (Color online) Example of the line-shape analysis of the 594 keV γ-ray transition and determination of the lifetime of the $I^{\pi} = (12^{+})$ level of the Band 1. On the left-hand side, spectra measured with the detectors of ring 7 and the fit (full line) are shown at three distances. The DSA portion of the fit is represented by a dash-dotted line, whereas the unshifted peak and the background are presented with a dashed line. The target-to-stopper distances and the corresponding mean end-of-flight times $\langle t_{f_f} \rangle$ are also indicated. The reduced χ^2 of the fit at all 15 distances is 1.08. On the right-hand side are displayed the τ curve (top), the numerator (middle), and the denominator (bottom) in Eq. (3). The straight line fitting the τ curve and its uncertainty limits are drawn through the sensitivity region. The derived lifetime and its statistical error are also displayed. See also the text.

equation:

$$S_{ij}^{\gamma}(E_\gamma) = \int_{-\infty}^{\infty} dE'_\gamma \frac{c}{E_{\gamma_0}} \Phi(E'_\gamma, E_\gamma) \times \int_0^{\infty} dt\, P_\theta[t, v_\theta(E'_\gamma)] b_{ij}\lambda_i n_i(t). \quad (4)$$

Here, the quantity $n_i(t)$ denotes the population of the level i as a function of the time t, λ_i is the decay constant of that level, and b_{ij} is the branching of the de-exciting transition $i \rightarrow j$. The stopping matrix $P_\theta(t, v_\theta)$ represents the normalized distributions of the velocity projection v_θ at different time steps. Depending on the experimental setup, additional corrections for geometry, efficiency, angular correlation, and kinematics effects (cf. Ref. [32]) have also to be taken into account in Eq. (4). Our approach for analyzing the line shapes and deriving lifetimes is presented in Refs. [24,28]. To use Eq. (4), it is necessary to determine via a Monte Carlo simulation the stopping matrix $P_\theta(t, v_\theta)$ that describes the stopping process. The line-shape analysis consists of solving Eq. (4) with respect to the decay function $b_{ij}\lambda_i n_i(t)$ of the transition $i \rightarrow j$. Finally, the lifetime $\tau_i = 1/\lambda_i$ of the level of interest i is extracted whereby the influence of the higher-lying feeding levels has also to be taken into account.

To obtain the line shapes of the investigated γ-ray transitions in both chiral candidate bands of ^{134}Pr, as already mentioned, gates were set in the γ-γ coincidence matrices on both shifted (S) and unshifted (U) components of lower-lying γ-ray transitions. The aim is the determination of the decay function $b_{ij}\lambda_i n_i(t)$ in Eq. (4) as a whole, i.e., of its numerical values as a function of the time t. We consider Eq. (4) as an integral equation for the decay function and describe its solution by a set of second-order polynomials over separate time intervals that are smoothly interconnected at the interval borders. The line-shape analysis is performed by varying the number and positions of the time borders until the best χ^2 fit of the line shape is obtained. The correlation matrix of the fit allows the determination of the statistical uncertainties in all subsequent calculations. In Fig. 4, the procedure is illustrated

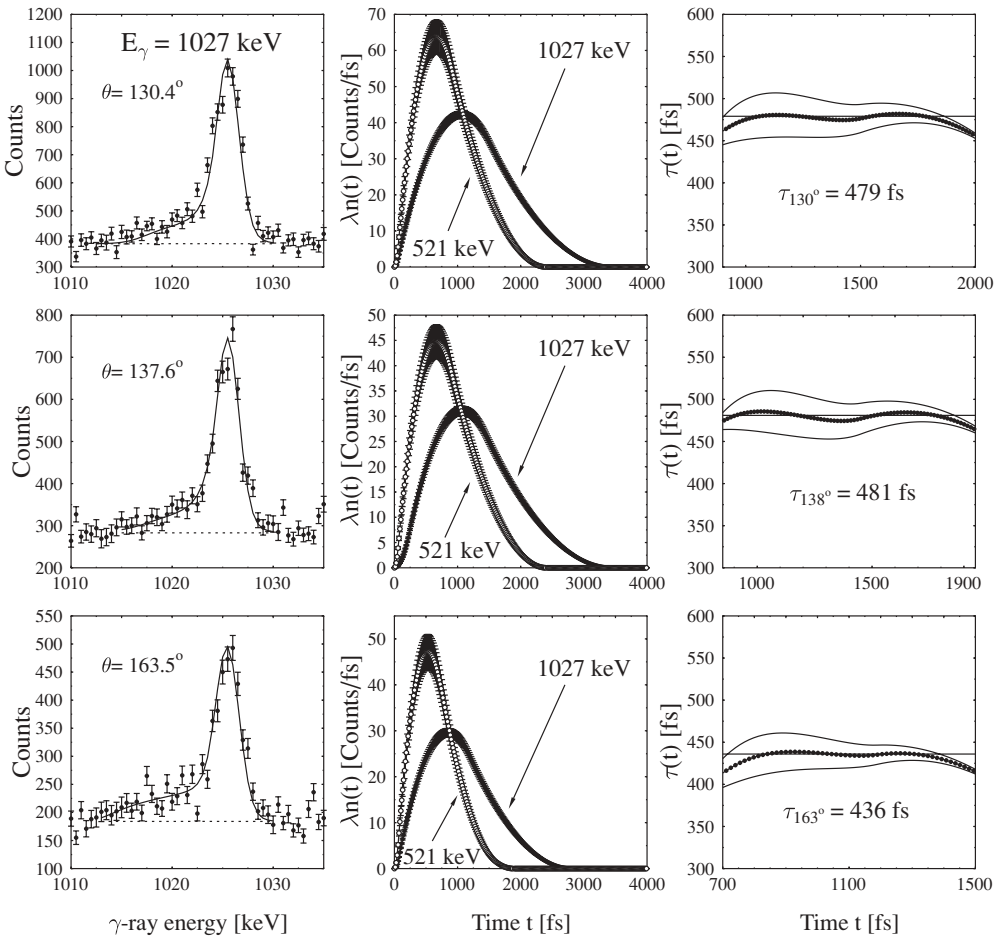

FIG. 4. Line-shape analysis of the 1027 keV transition in the Band 1 and determination of the lifetime of the $I^\pi = (17_1^+)$ level according to DDCM [24]. On the left-hand side are shown fits of the line shapes measured at the angles of 130.4°, 137.6°, and 163.5° with respect to the beam axis. The decay functions yielding the fits displayed in the left part are presented in the middle with their statistical uncertainties. The decay function of the feeding transition of 521 keV is also shown as determined from independent fits at the different detector angles. Its area is normalized to that of the decay function of the 1027 keV transition. The τ curves and their statistical uncertainties calculated with the decay functions shown in the middle of the figure are presented on the right-hand side. The lifetimes τ_θ derived at the three detector angles are also displayed.

for the 1027 keV transition in the Band 1 at three different detector angles. The fits of the line shapes are displayed in the left-hand part. In the middle, the decay functions of the transition corresponding to the best fits are presented with their statistical uncertainties.

The line-shape analysis yields the decay functions of the level of interest i and of the feeding levels h. When they are determined, the lifetime τ can be calculated according to the formalism of the DDCM [23] presented for the DSAM case in Ref. [24]:

$$\tau_i(t) = \frac{-\lambda_i \int_0^t dt' n_i(t') + \sum_h b_{hi}\lambda_h \int_0^t dt' n_h(t')}{\lambda_i n_i(t)}, \qquad (5)$$

where the summation over h includes all direct feeders of the level i and automatically takes into account the feeding history. Because the lifetime τ is a constant, the function $\tau_i(t)$, i.e., the τ curve given by Eq. (5), should represent a straight line when plotted versus the time t. Actually, this is realized only within some "region of sensitivity" where the values of the numerator and of the denominator in Eq. (5) are not too small. As discussed for the RDDS analysis, the deviations of the τ curve from a constant behavior within the sensitivity region immediately indicate the existence of systematic errors in the analysis. In each of the detector rings 1, 5, 6, 7, 8, 9, and 10, the line-shape analysis and the lifetime determination were performed independently. Because Eq. (5) implies a knowledge of all direct feeders, we had to investigate the intensity balance at the levels of interest as well. The intensities of the γ rays involved in the analysis were derived using the full statistics matrix that registers coincidences between any pair of detectors of EUROBALL and the ^{152}Eu efficiency calibration. The different positions of the detector rings with respect to the beam axis nearly ensure a smoothing of the angular correlation of the coincident γ rays that allows the derivation of the intensities within a good approximation. Due to the use of gates set on lower-lying transitions, it turned out that some unknown or side-feeding is present at every investigated level. Therefore, we adopted an often applied hypothesis on the time-behavior of the side-feeding, namely that it is the same as that of the known feeding. In addition, we investigated the influence of the side-feeding on the results obtained for the lifetimes (cf. below). To apply our hypothesis, the total intensity of the feeding decay functions was renormalized to the intensity of the depopulating decay function and the τ curves were calculated according to Eq. (5). Examples of τ curves obtained for the 1027 keV transition in the Band 1 at the three detector angles are shown in right-hand side of Fig. 4. (In the middle of this figure the decay functions used for the calculation of the τ values are displayed.) The weighted average values τ_θ within the sensitivity region and their statistical uncertainties $\Delta\tau_\theta$ were calculated using error propagation and taking into account the correlations between the different quantities participating in Eq. (5). The final result for τ was obtained as an unweighted mean of the values determined independently at the different angles (rings). For the uncertainty of its value, we adopted the square root of the variance of the results obtained at the seven different rings. We preferred this derivation of the mean value and its uncertainty because it better takes into account the systematic errors of the analysis at the individual rings (see also discussion of a similar problem in Ref. [28]).

The investigation of the uncertainties due to the side-feeding was done according to the approach outlined in Ref. [28].

Finally, we have investigated the effect of a possible incomplete knowledge of the stopping powers. For this purpose, we increased and decreased by 10% our basic set of stopping powers and reanalyzed some part of the data.

C. Determination of the branching ratios and polarization coefficients

In addition to the lifetimes we have determined in ^{134}Pr also the branching ratios and the electric or magnetic character of some transitions. The rings of clover detectors of the EUROBALL spectrometer, positioned at about 90° with respect to the beam, form a highly efficient Compton polarimeter [33,34]. The basic principle of the polarimeters is the dependence of the Compton scattering probability on the polarization of the γ rays emitted by oriented nuclei. This cross section described by the Klein-Nishina formula [35] shows a maximum in directions perpendicular to the incident polarization. Experimentally by Compton polarimeters we measure the scattering asymmetry A. The asymmetry is defined as $A = [a(E\gamma)N\perp - N||]/[a(E\gamma)N\perp + N||]$, where $N\perp$ and $N||$ are the numbers of counts registered by the orthogonally positioned Ge crystals in the Clover EUROBALL detectors and $a(E\gamma)$ is a normalization factor implying for the intrinsic asymmetry of the clover polarimeter. The scaling factor $a(E\gamma)$ is determined as a ratio of the coincidence events registered by the orthogonally positioned Ge crystals, measured without polarization at zero degree with respect to the beam. This scaling factor is a function of γ-ray energy. The values of $a(E\gamma)$ we have used to correct for the effect of intrinsic asymmetry are taken from Refs. [33,36]. A value of an $a(E\gamma) = 0.977(4)$ was obtained in Ref. [36] independent of $E\gamma$. This gives an idea about the size of the instrumental asymmetry.

The degree of polarization P is equal to A/Q, where Q is the polarimeter sensitivity. This sensitivity depends on the incident transition energy and the geometry of the experimental setup. The usual way to obtain the polarimeter sensitivity is to use a set of transitions of known polarization. In our analysis we used the polarization sensitivity curve determined in Ref. [34]. For the linear polarization investigations we created two coincidence γ-γ matrices. On the first axis of each of these two matrices γ-ray energy from all the Ge detectors of EUROBALL is sorted and on the second one is sorted the sum of two energy signals detected in two neighboring elements of the clover detectors, respectively, parallel or perpendicular to the beam direction. Setting conditions on the first axis, linear polarization results were obtained from the projected gates for all the γ-ray transitions of interest. An illustration of the investigations of the electric or magnetic character of the

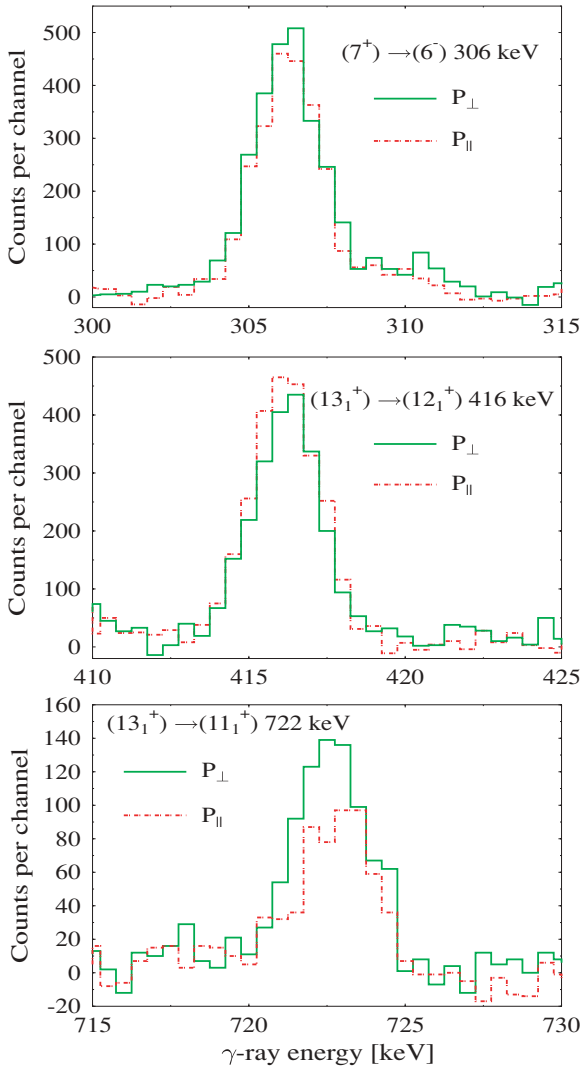

FIG. 5. (Color online) Comparison of the polarization experimental data for the $(7_1^+) \rightarrow (6_1^-)$, $(13_1^+) \rightarrow (12_1^+)$, $(13_1^+) \rightarrow (11_1^+)$ transitions.

transitions $(6_1^+) \rightarrow (6_1^-)$, $(13_1^+) \rightarrow (12_1^+)$, and $(13_1^+) \rightarrow (11_1^+)$ is presented in Fig. 5.

To determine branching ratios in ^{134}Pr, we have used the data from the DSAM measurement. Branching ratios were determined in both chiral candidates bands. For this purpose, spectra were obtained by gating on pure $E2$ transitions with $\Delta I = (I + 2 \rightarrow I)$ directly populating the level of interest. The gates were set in a coincidence matrix (122.6°, Σ) where the axis (Σ) corresponds to the detection of γ-rays by every detector of EUROBALL. Using such a gate, the gated spectra represent the γ-rays observed by the detectors of ring 5 at 122.6°.

An efficiency correction was applied using the results of the already mentioned calibration with a ^{152}Eu source. The final values of the intensities, corrected for angular correlation effects are presented in Table I. They were used for the determination of the branching ratios employed for the calculation of reduced transition probabilities.

IV. RESULTS

The lifetimes of the levels with $I^\pi = 10^+$ to 18^+ in Band 1 and with $I^\pi = 13^+$ to 17^+ in Band 2 have been derived. Except for the lifetime of the $I^\pi = 10^+$ in Band 1 [37] all the others are determined for the first time. The results of the analysis are presented in the recently published work [20]. We observe an excellent agreement between the lifetime value $\tau = 4.96(11)$ ps for $I^\pi = 10^+$ in Band 1, reported in the Ref. [37], and the value $\tau = 4.93(15)$ ps determined by us. The lifetimes of the states with $I^\pi = 10^+$ to 13^+ in Band 1 and with $I^\pi = 13^+$ to 14^+ in Band 2 have been determined from the RDDS part of the experiment. The other lifetimes are derived from the DSAM measurement.

The lifetimes for the states 14_1^+ and 15_2^+ have been determined from both the RDDS and DSAM experiments. For the state 14_1^+ we extract a lifetime value of 0.802(172) ps from the RDDS data, whereas from the DSAM measurements it is of 0.882(147) ps. For the state 15_2^+ we obtained respectively from RDDS 0.853(89) ps and from DSAM 0.897(47) ps. The results show a very good agreement within the error. We choose to present the values from the DSAM measurement for these two states because in this case the statistics is better. The DSAM part of the measurement was carried out for 96 h and every distance run in the RDDS part was carried out for 12 h. Moreover, due to the short lifetimes of the two states only four distances are in the sensitive region for the lifetime determination, making the DSAM results more reliable.

The derived lifetimes are presented in Table II. The $B(E2)$ and $B(M1)$ values obtained on the basis of the experimentally determined lifetimes and branching ratios are also shown in the same table where they are compared with the theoretically predicted values.

In addition to the measurement of lifetimes, the good statistics and high resolution of our data enabled us to precisely determine branching ratios (see also the previous section) for the decay of the populated levels. Almost all branching ratios reported in Ref. [17] were revised. We also observed new transitions, depopulating the levels with $I^\pi = 16^+$, $I^\pi = 17^+$, $I^\pi = 18^+$ in Band 1, reported in Ref. [27], and this fact changes the values of the branching ratios reported in Ref. [17]. All derived new values for the branching ratios are presented in Table I. Also the level scheme of the ^{134}Pr was reinvestigated. We confirmed that the delayed component of the 306 keV doublet has an $E1$ character. Our result can be seen in Fig. 5. The fact that the transition $7_1^+ \rightarrow 6_1^-$ is an $E1$ transition has been reported by Roberts *et al.* [38].

In the partial level scheme of ^{134}Pr, shown in Fig. 1, the 39 keV transition $(8_1^+ \rightarrow 7_1^+)$ reported in Ref. [38] is also presented, which, due to the low energy, is not observed in our experiment. For the in-band transitions with $\Delta I = 1$, it was found that they have $M1$ character with a negligible $E2$ component. The in-band transitions with $\Delta I = 2$ show $E2$ character. The interband transitions with $\Delta I = 2$ have an $E2$ character and the interband transitions with $\Delta I = 1$ show a mixed $M1 + E2$ character. The linear polarizations coefficients are reported in Table I. The statistics in our experiment were not sufficient for the determination of the mixing ratios of the $M1 + E2$ interband transitions.

TABLE I. Intensities, polarization coefficients, and γ multipolarities of transitions in ^{134}Pr. The first column identifies transitions by the spin/parity assignments I_k^π of the initial and final states. The index k is the label of the band. The experimental γ energies are given in the second column. The experimentally derived intensities and the theoretically calculated ones by the IBFFM and the TQPTR are presented in the next three columns. In the last two columns are shown experimentally derived polarization coefficients and γ multipolarities assigned.

Transition	E_γ(keV)	I_γ^{Exp}	I_γ^{IBFFM}	I_γ^{TQPTR}	Pol.	γ mult.
$7_1^+ \to 6_1^-$	306.5	100.0(10)			0.19(4)	$E1$
$8_1^+ \to 7_1^+$	39.3	100[a]	100			$M1+E2$
$9_1^+ \to 8_1^+$	94.3	100.0(10)	100	100	−0.22(5)	$M1+E2$
$9_1^+ \to 7_1^+$			0.3			$E2$
$10_1^+ \to 9_1^+$	171.0	100.0(10)	100	100	−0.10(4)	$M1+E2$
$10_1^+ \to 8_1^+$			2.1	0.8		$E2$
$11_1^+ \to 10_1^+$	287.4	100.0(10)	100	100	−0.11(4)	$M1+E2$
$11_1^+ \to 9_1^+$	458.1	12.9(7)	8.0	3.7	0.50(8)	$E2$
$11_1^+ \to 9_2^+$			0.0	0.0		$E2$
$12_1^+ \to 11_1^+$	306.2	100.0(10)	100	100		$M1+E2$
$12_1^+ \to 10_1^+$	593.6	34.0(5)	34.9	9.7	0.58(7)	$E2$
$12_1^+ \to 10_2^+$			0.0	0.1		$E2$
$12_1^+ \to 11_2^+$				0.1		$M1+E2$
$13_1^+ \to 12_1^+$	416.2	100.0(10)	100	100	−0.24(5)	$M1+E2$
$13_1^+ \to 11_1^+$	722.4	50.6(9)	44.5	15.9	0.81(8)	$E2$
$13_1^+ \to 12_2^{+\,b}$	103.1	<0.8	0.0	0.6		$M1+E2$
$13_1^+ \to 11_2^{+\,b}$	386.1	<9.2	0.2	1.0		$E2$
$14_1^+ \to 13_1^+$	395.3	68.9(10)	87.6	86.0	−0.10(5)	$M1+E2$
$14_1^+ \to 12_1^+$	811.5	100.0(10)	100	100	0.88(8)	$E2$
$14_1^+ \to 13_2^{+\,b}$	174.8	<1.7	0.2	36.3		$M1+E2$
$14_1^+ \to 12_2^{+\,b}$	498.4	<11.8	0.3			$E2$
$15_1^+ \to 14_1^+$	495.3	61.2(10)	87.7	100	−0.35(9)	$M1+E2$
$15_1^+ \to 13_1^+$	890.3	100.0(14)	100	78.7	0.4(1)	$E2$
$15_1^+ \to 14_2^{+\,b}$	333.1	<1.8	1.3	4.3		$M1+E2$
$15_1^+ \to 13_2^{+\,b}$	670.1	<11.3	0.6	5.1		$E2$
$16_1^+ \to 15_1^+$	480.6	22.9(7)	49.8	52.8	−0.10(8)	$M1+E2$
$16_1^+ \to 14_1^+$	975.6	100.0(12)	100	100	0.8(3)	$E2$
$16_1^+ \to 15_2^+$	443.0	18.8(6)	1.5	32.5	−0.5(3)	$M1+E2$
$16_1^+ \to 14_2^{+\,b}$	813.7	<12.8	0.0	18.4		$E2$
$16_1^+ \to 16_2^+$			0.0	0.0		$M1+E2$
$17_1^+ \to 16_1^+$	546.1	37.0(10)	21.2	67.1	−0.3(1)	$M1+E2$
$17_1^+ \to 15_1^+$	1026.8	100.0(18)	100	83.8	1.0(2)	$E2$
$17_1^+ \to 15_2^+$	989.0	19.7(8)	11.5	100	0.5(2)	$E2$
$17_1^+ \to 16_2^{+\,b}$	591.4	<1.4	33.8	0.5		$M1+E2$
$17_1^+ \to 17_2^+$			0.0	0.0		$M1+E2$
$18_1^+ \to 17_1^+$	520.8	29.2(11)		0.8	−0.7(2)	$M1+E2$
$18_1^+ \to 16_1^+$	1067.0	100.0(21)		100	0.6(2)	$E2$
$18_1^+ \to 16_2^+$	1110.0	31.1(12)		0.3	0.7(2)	$E2$
$18_1^+ \to 17_2^{+\,b}$	640.2	<1.6		61.2		$M1+E2$
$18_1^+ \to 18_2^+$				0.1		$M1+E2$
$6_2^+ \to 8_1^+$			0.4			$E2$
$6_2^+ \to 7_1^+$			100			$M1+E2$
$7_2^+ \to 6_2^+$			5.2			$M1+E2$
$7_2^+ \to 8_1^+$			100			$M1+E2$
$7_2^+ \to 7_1^+$			0.1			$M1+E2$

TABLE I. *(Continued.)*

Transition	E_γ(keV)	I_γ^{Exp}	$I_\gamma^{\mathrm{IBFFM}}$	$I_\gamma^{\mathrm{TQPTR}}$	Pol.	γ mult.
$8_2^+ \to 9_1^+$	257.0	Seen	36.3	100		$M1+E2$
$8_2^+ \to 7_1^+$	390.0	Seen	100			$M1+E2$
$8_2^+ \to 8_1^+$			0.2	2.5		$M1+E2$
$8_2^+ \to 10_1^+$			0.0	0.0		$E2$
$8_2^+ \to 7_2^+$			3.4			$M1+E2$
$8_2^+ \to 6_2^+$			0.0			$E2$
$9_2^+ \to 8_2^+$	167.0	Seen	15.3	18.9		$M1+E2$
$9_2^+ \to 10_1^+$			7.9	3.5		$M1+E2$
$9_2^+ \to 9_1^+$			1.5	0.4		$M1+E2$
$9_2^+ \to 8_1^+$	518.0	100(15)	100	100		$M1+E2$
$9_2^+ \to 7_1^+$			0.0			$E2$
$9_2^+ \to 7_2^+$			0.0			$E2$
$10_2^+ \to 9_2^+$	204.0	Seen	26.8	30.2		$M1+E2$
$10_2^+ \to 8_2^+$			2.9	0.7		$E2$
$10_2^+ \to 8_1^+$	722.0	Seen	1.6	15.7		$E2$
$10_2^+ \to 9_1^+$	628.0	100.0(12)	100	100	−0.4(2)	$M1+E2$
$10_2^+ \to 10_1^+$	457.0	Seen	2.8	2.4		$M1+E2$
$10_2^+ \to 11_1^+$	170.0	Seen	1.9	0.3		$M1+E2$
$11_2^+ \to 10_2^+$	167.0	Seen	26.8	51.7		$M1+E2$
$11_2^+ \to 9_2^+$			6.0	1.9		$E2$
$11_2^+ \to 9_1^+$	795.0	Seen	53.8	39.2	0.3(2)	$E2$
$11_2^+ \to 10_1^+$	624.0	100.0(10)	100	100	−0.3(1)	$M1+E2$
$11_2^+ \to 11_1^+$			1.7	1.4		$M1+E2$
$11_2^+ \to 12_1^+$			0.0			$M1+E2$
$12_2^+ \to 11_2^+$	283.0	83.9(10)	83.9	83.9	−0.2(1)	$M1+E2$
$12_2^+ \to 10_2^+$			3.0	5.2		$E2$
$12_2^+ \to 10_1^+$	907.0	23.2(8)	102	45.3	0.4(2)	$E2$
$12_2^+ \to 11_1^+$	620.0	100.0(10)	72.3	56.7	−0.2(1)	$M1+E2$
$12_2^+ \to 12_1^+$			0.2	0.2		$M1+E2$
$13_2^+ \to 12_2^+$	323.6	100.0(10)	100	100	−0.3(1)	$M1+E2$
$13_2^+ \to 11_2^+$			0.0	24.4		$E2$
$13_2^+ \to 12_1^+$	637.5	33.4(10)	25.2	37.0	−0.2(1)	$M1+E2$
$13_2^+ \to 11_1^+$	944.0	5.7(5)	39.3	81.9	0.9(3)	$E2$
$13_2^+ \to 13_1^+$			0.0	0.1		$M1+E2$
$14_2^+ \to 13_2^+$	337.0	100.0(12)	100	100	−0.2(1)	$M1+E2$
$14_2^+ \to 12_2^+$	661.0	13.2(9)	35.4	84.9	0.8(2)	$E2$
$14_2^+ \to 13_1^+$	558.1	42.2(10)	10.3	275.0	−0.3(2)	$M1+E2$
$14_2^+ \to 12_1^+$	975.1	10.4(5)	69.8	20.5	0.8(3)	$E2$
$14_2^+ \to 14_1^+$			0.0	0.0		M1+E2
$15_2^+ \to 14_2^+$	368.8	100.0(15)	100	100	−0.2(1)	$M1+E2$
$15_2^+ \to 13_2^+$	705.8	46.0(10)	36.6	70.5	0.3(2)	$E2$
$15_2^+ \to 14_1^+$	531.3	70.2(12)	11.8	8.0	−0.3(2)	$M1+E2$
$15_2^+ \to 13_1^+$	927.2	49.7(11)	13.2	11.8	0.4(2)	$E2$
$15_2^+ \to 15_1^+$			0.0	0.0		$M1+E2$
$16_2^+ \to 15_2^+$	399.6	90.2(13)	90.2	90.2	−0.4(2)	$M1+E2$
$16_2^+ \to 14_2^+$	768.4	39.7(10)	70.2	245.2	0.2(1)	$E2$
$16_2^+ \to 15_1^+$	436.2	100.0(16)	2.4	132.4	−0.3(1)	$M1+E2$

TABLE I. *(Continued.)*

Transition	E_γ(keV)	I_γ^{Exp}	I_γ^{IBFFM}	I_γ^{TQPTR}	Pol.	γ mult.
$16_2^+ \rightarrow 14_1^+$	931.0	57.5(12)	72.2	85.2	0.3(2)	$E2$
$17_2^+ \rightarrow 16_2^+$	472.0	100.0(18)	100	100	−0.4(2)	$M1+E2$
$17_2^+ \rightarrow 15_2^+$	872.0	28.6(12)	36.1	55.0	0.6(4)	$E2$
$17_2^+ \rightarrow 16_1^+$	428.0	70.3(14)	78.8	0.9	−0.4(2)	$M1+E2$
$17_2^+ \rightarrow 15_1^+$	907.8	78.9(14)	44.2	98.0	0.2(1)	$E2$

[a]The presence of 39 keV transition ($8_1^+ \rightarrow 7_1^+$) has been reported in Ref. [38].

[b]Transition not observed in the data. The energy of the transition is obtained from the corresponding experimental level energies. The estimation of the limit of the relative intensity is obtained from the background investigation. See also the text.

V. DISCUSSION

The energies and electromagnetic transition probabilities of the chiral candidate bands in ^{134}Pr are calculated both in the framework of the two-quasiparticle triaxial rotor model (TQPTR) as described in Refs. [1,39] and of the IBFFM [40,41].

A. TQPTR calculations

The TQPTR model assumes a rigid triaxial shape. The orientation angles of the angular momentum with respect to this shape are the only degrees of freedom. The deformation parameters and the pair gaps were chosen the same as calculated in Ref. [2] by means of the tilted axis cranking (TAC) approach, which demonstrated the existence of chiral mean field solution around $I = 15$ for ^{134}Pr. In contrast to conventional TQPTR calculations as in Ref. [1] or to the equivalent Kerman-Klein-Dönau-Frauendorf (KKDF) calculations in, e.g., Ref. [8], the ratio between the three moments of inertia was calculated by means of cranking the triaxial potential about the three principal axes with the rotational frequency ω. The parameters of the mean field were kept constant and equal to ones found in the TAC calculation [2]. Our calculation gave nearly linear functions of the angular-momentum expectation values $\langle J_s\rangle$, $\langle J_i\rangle$, $\langle J_l\rangle$, where s, i, l denote the short, intermediate, and long axes, respectively. The moments of inertia were taken from the slopes. The ratios between these microscopic moments of inertia were $\mathcal{J}_s/\mathcal{J}_l = 1.52$ and $\mathcal{J}_i/\mathcal{J}_l = 3.55$, which differ from the respective ratios of 1 and 4 obtained assuming irrotational flow. The overall scale of the moments of inertia was adjusted to the 2^+ energy of the even-even neighbors.

Figure 6 shows the comparison of the experimentally measured level scheme with the results of the TQPTR calculations. The overall agreement obtained between theory and experiment for level energies and branching ratios is remarkable. One notices in particular the good agreement obtained between the experimental and theoretical level energies in the medium- and high-spin regions.

B. IBFFM calculations

This model is based on the interacting boson model (IBM-1) [42,43] for even-even nuclei and the interacting boson-fermion model (IBFM-1) [44,45] for odd-A nuclei. A detailed procedure of this calculation and the parameter choice can be found in Ref. [19]. The IBFFM description of the chiral candidate bands in ^{134}Pr is fully consistent with the IBM-1/IBFM-1 calculations for its even-even (^{134}Ce) and odd-even (^{135}Pr and ^{133}Ce) neighbors. In Ref. [19] the theoretical predictions have been compared to experimental data from Ref. [17]. Based on the present experimental data some parameters are now determined much more accurately. The agreement with the experimental spectrum is improved by excluding the residual odd proton-odd neutron quadrupole-quadrupole interaction ($V_2 = 0$ MeV) and with a fine-tuning of the parameters $A_0^\pi = 0.07$ MeV, $\chi = -0.6$, and $\eta = -0.35$ MeV of the IBFM Hamiltonian described in Ref. [19].

These values of χ and η are consistently used in the boson quadrupole operator appearing in the boson-fermion dynamical interaction, as well as in the $E2$ operator. In Fig. 7 the two lowest calculated positive-parity bands in ^{134}Pr, based on negative-parity orbitals of the odd proton and odd neutron, are shown in comparison with the experimental bands. We note that in Ref. [19] it was stated that 7^+ is the lowest calculated member of the $\pi h_{11/2} \otimes \nu h_{11/2}$ configuration in agreement with the experimental results. The effective charges and gyromagnetic ratios in Ref. [19] have been chosen on the basis of some other IBFM/IBFFM calculations in the region and of the branching ratios in ^{134}Pr [17]. A better agreement with the present $B(E2)$ and $B(M1)$ values has required the adjustment of one of the parameters in both electromagnetic operators. The boson charge is fixed to $e^{\text{vib}} = 1.2$ (i.e., to the value that gives the best fit of $E2$ properties in the core nucleus) and the boson gyromagnetic factor is reduced to one-third of the hydrodynamic estimate $g_R = \frac{1}{3}(\frac{Z}{A}) = 0.15$. Magnetic moments for the 2^+ states in the even-even Ce isotopes are experimentally not known. From experimental data in even-even Xe and Ba nuclei, boson gyromagnetic factors in IBM-1 in the range 0.34–0.42 can be deduced. In the IBFM-1 calculations for odd-mass Xe and Ba isotopes in this region, a smaller value of boson g-factor $g_R = 0.25$ [46] has been used. The microscopically derived IBM-2 boson g-factors for Xe isotopes [47], with values of $\approx$0.85 for proton bosons and ≈ -0.2 for neutron bosons, may indicate that in this region of soft nuclei the neutron contribution to the boson g-factor in IBM-1 can lead to a sizable quenching of the $g_R = \frac{Z}{A} \approx 0.45$ estimate in odd-A nuclei.

TABLE II. Electromagnetic transition properties of states in ^{134}Pr. The first column identifies the transitions by their initial and final angular momentum and parity assignments I_k^π. The index k is the label of the band. The derived lifetimes and the experimental and theoretical values of the $B(E2)$ and $B(M1)$ transition probabilities are presented in the next columns.

Transition	τ (ps)	$B(E2)^{\text{exp}}$ (e^2b^2)	$B(E2)^{\text{IBFFM}}$ (e^2b^2)	$B(E2)^{\text{TQPTR}}$ (e^2b^2)	$B(M1)^{\text{exp}}$ (μ_N^2)	$B(M1)^{\text{IBFFM}}$ (μ_N^2)	$B(M1)^{\text{TQPTR}}$ (μ_N^2)
$8_1^+ \to 7_1^+$			0.245			1.396	
$9_1^+ \to 8_1^+$			0.232	0.454		1.151	1.888
$9_1^+ \to 7_1^+$			0.109				
$10_1^+ \to 9_1^+$	4.93(15)		0.228	0.454	1.788(57)	1.067	1.751
$10_1^+ \to 8_1^+$			0.125	0.070			
$11_1^+ \to 10_1^+$	1.614(326)		0.219	0.436	1.235(65)	0.911	1.591
$11_1^+ \to 9_1^+$		0.268(33)	0.125	0.089			
$11_1^+ \to 9_2^+$			0.031	0.017			
$12_1^+ \to 11_1^+$	1.425(130)		0.191	0.414	0.991(74)	0.755	1.563
$12_1^+ \to 10_1^+$		0.198(29)	0.151	0.108			
$12_1^+ \to 10_2^+$			0.024	0.029			
$12_1^+ \to 11_2^+$				0.003			0.233
$13_1^+ \to 12_1^+$	0.904(50)		0.161	0.400	0.568(65)	0.711	1.503
$13_1^+ \to 11_1^+$		0.151(27)	0.172	0.102			
$13_1^+ \to 12_2^+$			0.002	0.001	<0.34	0.019	0.095
$13_1^+ \to 11_2^+$		<0.66	0.020	0.056			
$14_1^+ \to 13_1^+$	0.882(147)		0.136	0.193	0.419(85)	0.573	0.691
$14_1^+ \to 12_1^+$		0.153(21)	0.170	0.204			
$14_1^+ \to 12_2^+$		<0.24	0.006	0.000			
$14_1^+ \to 13_2^+$			0.000	0.100	<0.14	0.013	0.9
$15_1^+ \to 14_1^+$	0.608(68)		0.096	0.263	0.290(80)	0.521	1.436
$15_1^+ \to 13_1^+$		0.148(21)	0.192	0.207			
$15_1^+ \to 13_2^+$		<0.077	0.005	0.031			
$15_1^+ \to 14_2^+$			0.005	0.002	<0.032	0.027	0.087
$16_1^+ \to 15_1^+$	0.562(47)		0.085	0.133	0.146(70)	0.426	0.557
$16_1^+ \to 14_1^+$		0.115(19)	0.160	0.213			
$16_1^+ \to 15_2^+$			0.001	0.071	<0.17	0.017	0.485
$16_1^+ \to 14_2^+$		<0.035	0.000	0.049			
$16_1^+ \to 16_2^+$			0.000	0.001		0.000	0.005
$17_1^+ \to 16_1^+$	0.422(30)		0.012	0.205	0.194(70)	0.168	1.307
$17_1^+ \to 15_1^+$		0.108(22)	0.165	0.141			
$17_1^+ \to 15_2^+$		0.026(3)	0.023	0.224			
$17_1^+ \to 16_2^+$			0.036	0.005	<0.0073	0.208	0.003
$17_1^+ \to 17_2^+$			0.002	0.005		0.001	0.008
$18_1^+ \to 17_1^+$	0.249(10)			0.001	0.292(57)		0.015
$18_1^+ \to 16_1^+$		0.147(27)		0.357			
$18_1^+ \to 16_2^+$		0.038(3)		0.001			
$18_1^+ \to 17_2^+$				0.126	<0.0096		0.693
$18_1^+ \to 18_2^+$				0.000			0.023
$19_1^+ \to 18_1^+$				0.105			0.802
$19_1^+ \to 17_1^+$				0.442			
$19_1^+ \to 17_2^+$				0.007			
$19_1^+ \to 18_2^+$				0.000			0.006
$19_1^+ \to 19_2^+$				0.004			0.012
$20_1^+ \to 19_1^+$				0.000			0.000
$20_1^+ \to 18_1^+$				0.452			
$20_1^+ \to 18_2^+$				0.000			
$20_1^+ \to 19_2^+$				0.086			0.510

TABLE II. *(Continued.)*

Transition	τ (ps)	$B(E2)^{\text{exp}}$ (e^2b^2)	$B(E2)^{\text{IBFFM}}$ (e^2b^2)	$B(E2)^{\text{TQPTR}}$ (e^2b^2)	$B(M1)^{\text{exp}}$ (μ_N^2)	$B(M1)^{\text{IBFFM}}$ (μ_N^2)	$B(M1)^{\text{TQPTR}}$ (μ_N^2)
$20_1^+ \rightarrow 20_2^+$				0.002			0.054
$21_1^+ \rightarrow 20_1^+$				0.031			0.231
$21_1^+ \rightarrow 19_1^+$				0.505			
$21_1^+ \rightarrow 19_2^+$				0.001			
$21_1^+ \rightarrow 20_2^+$				0.000			0.010
$21_1^+ \rightarrow 21_2^+$				0.003			0.015
$8_2^+ \rightarrow 10_1^+$			0.014	0.015			
$8_2^+ \rightarrow 9_1^+$			0.003	0.005		0.572	0.566
$8_2^+ \rightarrow 7_1^+$			0.004			0.451	
$8_2^+ \rightarrow 8_1^+$			0.005	0.041		0.001	0.002
$9_2^+ \rightarrow 8_2^+$			0.094	0.362		0.603	2.237
$9_2^+ \rightarrow 10_1^+$			0.000	0.001		0.148	0.399
$9_2^+ \rightarrow 9_1^+$			0.017	0.028		0.004	0.002
$9_2^+ \rightarrow 8_1^+$			0.017	0.037		0.216	0.465
$9_2^+ \rightarrow 8_2^+$			0.094	0.362		0.603	2.237
$9_2^+ \rightarrow 10_1^+$			0.000	0.001		0.148	0.399
$9_2^+ \rightarrow 9_1^+$			0.017	0.028		0.004	0.002
$9_2^+ \rightarrow 8_1^+$			0.017	0.037		0.216	0.465
$9_2^+ \rightarrow 7_1^+$			0.000				
$10_2^+ \rightarrow 11_1^+$			0.001	0.004		0.065	0.384
$10_2^+ \rightarrow 9_2^+$			0.076	0.319		0.518	1.760
$10_2^+ \rightarrow 8_2^+$			0.097	0.090			
$10_2^+ \rightarrow 10_1^+$			0.013	0.032		0.003	0.021
$10_2^+ \rightarrow 9_1^+$			0.006	0.030		0.065	0.244
$10_2^+ \rightarrow 8_1^+$			0.002	0.090			
$11_2^+ \rightarrow 12_1^+$			0.006			0.129	
$11_2^+ \rightarrow 10_2^+$			0.050	0.295		0.587	1.708
$11_2^+ \rightarrow 11_1^+$			0.008	0.031		0.004	0.021
$11_2^+ \rightarrow 9_2^+$			0.126	0.099			
$11_2^+ \rightarrow 10_1^+$			0.004	0.048		0.041	0.197
$11_2^+ \rightarrow 9_1^+$			0.025	0.094			
$12_2^+ \rightarrow 11_2^+$			0.063	0.303		0.532	1.525
$12_2^+ \rightarrow 12_1^+$			0.005	0.020		0.001	0.009
$12_2^+ \rightarrow 10_2^+$			0.034	0.105			
$12_2^+ \rightarrow 11_1^+$			0.022	0.050		0.038	0.147
$12_2^+ \rightarrow 10_1^+$			0.035	0.082			
$13_2^+ \rightarrow 12_2^+$	1.443(50)		0.130	0.269	0.804(90)	0.651	1.338
$13_2^+ \rightarrow 11_1^+$		0.0030(5)	0.017	0.096			
$13_2^+ \rightarrow 12_1^+$			0.024	0.026	<0.037	0.015	0.098
$13_2^+ \rightarrow 11_2^+$			0.000	0.160			
$13_2^+ \rightarrow 13_1^+$			0.000	0.016		0.000	0.014
$14_2^+ \rightarrow 13_2^+$	1.280(50)		0.131	0.143	0.678(100)	0.538	0.765
$14_2^+ \rightarrow 12_2^+$		0.039(19)	0.085	0.252			
$14_2^+ \rightarrow 13_1^+$			0.011	0.208	<0.066	0.010	0.769
$14_2^+ \rightarrow 12_1^+$		0.0044(7)	0.024	0.015			
$14_2^+ \rightarrow 14_1^+$			0.000	0.000		0.000	0.000
$15_2^+ \rightarrow 14_2^+$	0.887(47)		0.091	0.256	0.472(90)	0.566	1.216
$15_2^+ \rightarrow 13_2^+$		0.089(20)	0.087	0.271			
$15_2^+ \rightarrow 14_1^+$			0.018	0.022	<0.12	0.019	0.072
$15_2^+ \rightarrow 13_1^+$		0.025(3)	0.008	0.021			

TABLE II. *(Continued.)*

Transition	τ (ps)	$B(E2)^{\text{exp}}$ (e^2b^2)	$B(E2)^{\text{IBFFM}}$ (e^2b^2)	$B(E2)^{\text{TQPTR}}$ (e^2b^2)	$B(M1)^{\text{exp}}$ (μ_N^2)	$B(M1)^{\text{IBFFM}}$ (μ_N^2)	$B(M1)^{\text{TQPTR}}$ (μ_N^2)
$15_2^+ \rightarrow 15_1^+$			0.000	0.000		0.000	0.000
$16_2^+ \rightarrow 15_2^+$	0.824(52)		0.061	0.118	0.333(75)	0.192	0.755
$16_2^+ \rightarrow 14_2^+$		0.050(18)	0.056	0.306			
$16_2^+ \rightarrow 15_1^+$			0.001	0.105	<0.30	0.004	0.728
$16_2^+ \rightarrow 14_1^+$		0.028(2)	0.021	0.083			
$17_2^+ \rightarrow 16_2^+$	0.353(49)		0.036	0.151	0.545(67)	0.206	1.288
$17_2^+ \rightarrow 15_2^+$		0.047(17)	0.023	0.176			
$17_2^+ \rightarrow 16_1^+$			0.048	0.002	<0.58	0.216	0.034
$17_2^+ \rightarrow 15_1^+$		0.105(30)	0.023	0.227			
$18_2^+ \rightarrow 17_2^+$				0.002			0.046
$18_2^+ \rightarrow 16_2^+$				0.465			
$18_2^+ \rightarrow 16_1^+$				0.000			
$18_2^+ \rightarrow 17_1^+$				0.171			1.571
$19_2^+ \rightarrow 18_2^+$				0.110			1.197
$19_2^+ \rightarrow 17_2^+$				0.511			
$19_2^+ \rightarrow 17_1^+$				0.009			
$19_2^+ \rightarrow 18_1^+$				0.000			0.005
$20_2^+ \rightarrow 19_2^+$				0.000			0.006
$20_2^+ \rightarrow 18_2^+$				0.526			
$20_2^+ \rightarrow 18_1^+$				0.000			
$20_2^+ \rightarrow 19_1^+$				0.139			1.697
$21_2^+ \rightarrow 20_2^+$				0.082			1.132
$21_2^+ \rightarrow 19_2^+$				0.579			
$21_2^+ \rightarrow 19_1^+$				0.001			
$21_2^+ \rightarrow 20_1^+$				0.000			0.002

The important feature of the IBFFM is the description of the even-even core. In the IBFFM the orientation of the angular momentum vector with respect to the deformed shape is not the only core degree of freedom because the deformation of the core is also taken as an additional degree of freedom. Valence quasiparticles in the IBFFM are coupled to all structures of the boson ^{134}Ce core (ground-state band, γ-band, $K = 0$ band, $K = 4$ band, ...) that are present in the basis limited by the total boson number.

Numerous IBM studies of even-even nuclei in the $A \approx 130$ mass region have shown that these nuclei are well described by the O(6) symmetry of the IBM, that in the classical limit corresponds to the Wilets-Jean model of a γ-unstable rotor [48], and that the accepted interpretation is that they are γ-soft. In the IBM-1 framework, where there is no distinction between proton bosons and neutron bosons, the standard boson Hamiltonian with up to two-body boson interactions can describe nuclei with axial, γ-unstable, or transitional shapes. Rigid triaxial nuclei can be described either in the proton-neutron IBM-2 framework or, considering higher-order interactions between bosons in IBM-1 (at least up to four-body) in the SU(3) limit, where triaxial states belonging to representations that are high in excitation energy can be brought lowest in energy [49], at least algebraically. For the standard boson IBM-1 Hamiltonian with one- and two-body interactions, triaxiality reduces to γ instability for finite boson systems [50,51]. For γ-unstable nuclei in the O(6) limit or close to it, the potential energy surface is flat in the γ direction but is also rather broad in the β direction. The wave functions are not (β, γ) dependent, but an *effective* γ_{eff} can be calculated [52] that for O(6) is 30°. It is the mean value in a given IBM-1 state calculated within the model (see Sec. V C). It is not the usual expectation value but the representative for an equivalent triaxially deformed rotor. In contrast to the triaxially deformed rotor, γ_{eff} *is not* the static geometrical deformation and the fluctuations of γ are very large [53]. In such a context the term *dynamical chirality*, which we shall use in the following, refers to the possibility that the angular momenta of the proton, neutron, and core in the odd-odd nucleus, find themselves in the favorable geometry, as if they would in the equivalent triaxially deformed rotor. The present calculation will show that such a possibility is present, but it is far from being dominant. The condition for the appearance of twin bands with wave functions realistic enough to reproduce the electromagnetic decay of the bands is that the core is a γ-unstable rotor whose effective γ is in the range of triaxial values. To reproduce the energy spectra of ^{134}Pr and its even-even isobar ^{134}Ce, in the present calculation a cubic (three-body) term [54,55] is added to the standard IBM-1 Hamiltonian. This term generates a triaxial equilibrium deformation, but the minimum is still broad [54]

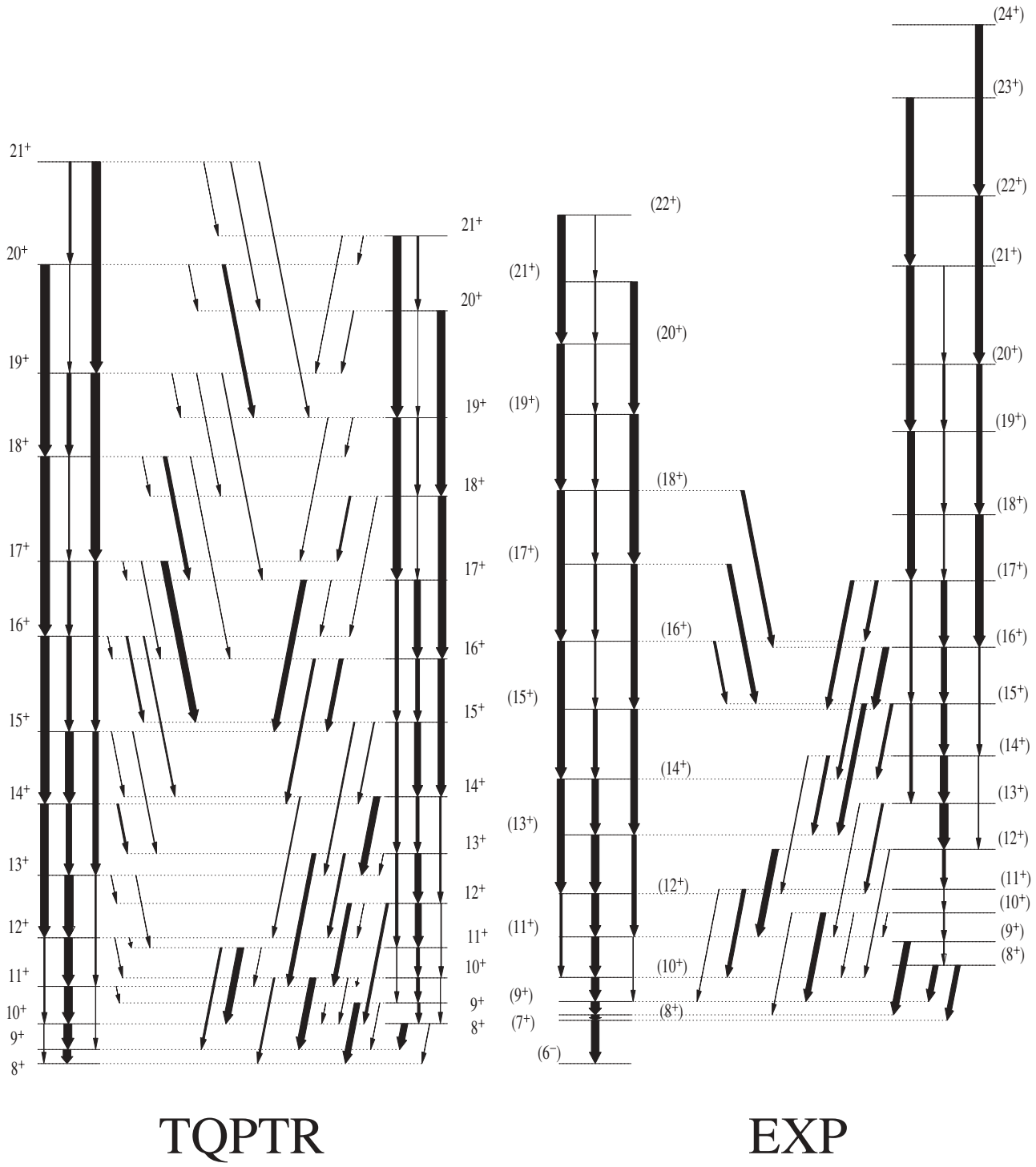

FIG. 6. Comparison of the experimental bands in ^{134}Pr with the lowest two bands calculated in the TQPTR. The thickness of the arrows corresponds to the relative γ intensity in each branch.

and the fluctuations of the shape are large. We notice that the parametrization for the IBM and IBFFM Hamiltonians and for electromagnetic operators in the present work is the one used in Ref. [20].

In Fig. 7 the experimental branching ratios and the ones calculated within the IBFFM are shown. The calculated in-band and interband decay patterns of both bands agree well with the observed ones. For many branches the agreement is almost perfect. For levels with lower spins, the experimental $B(E2)$ and $B(M1)$ values are not known, but on the basis of the agreement between theory and experiment for branching ratios, it can be expected that they will be in the range of

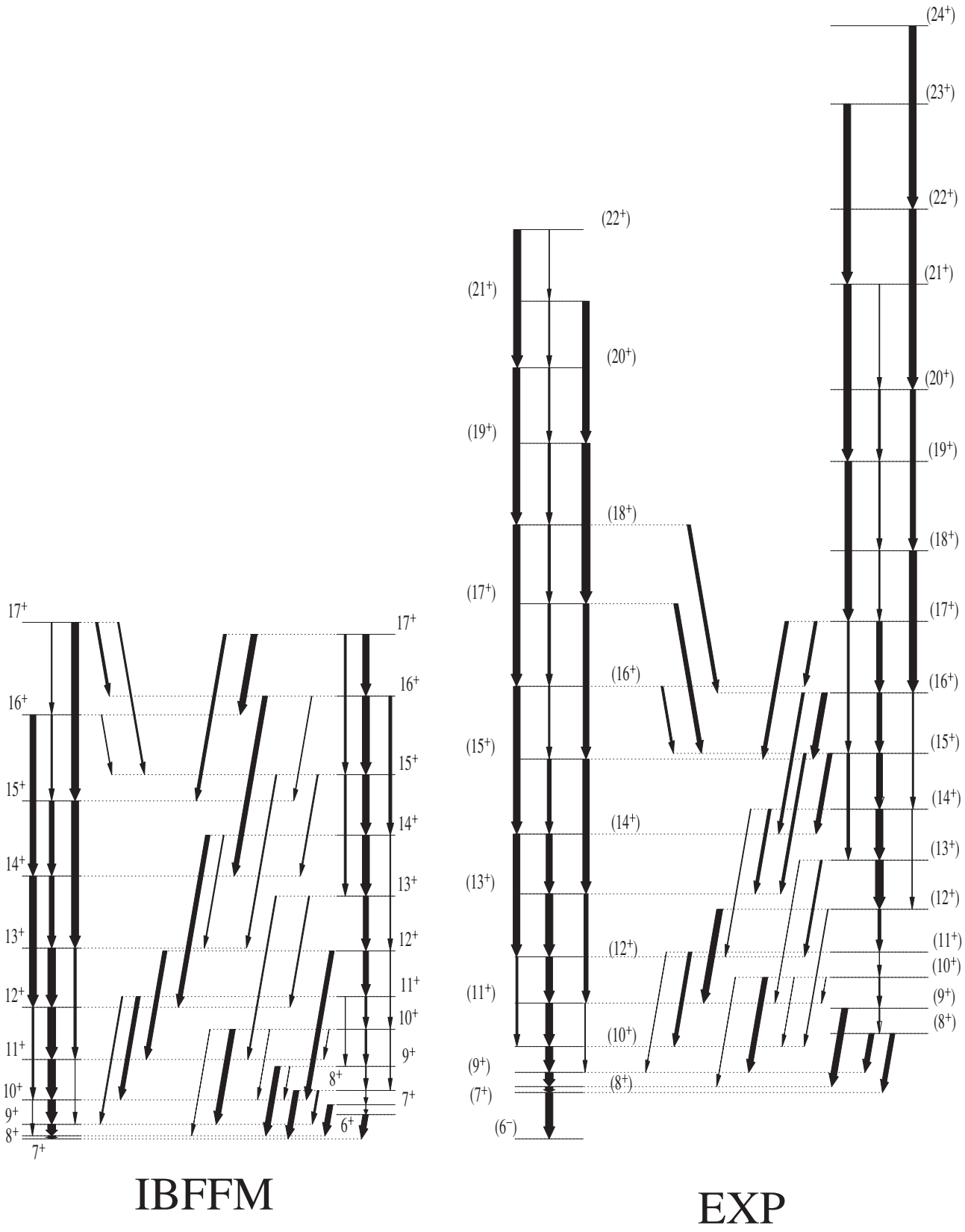

FIG. 7. Comparison of the experimental bands in ^{134}Pr with the lowest two bands calculated in the IBFFM. The thickness of the arrows corresponds to the relative γ intensity in each branch.

IBFFM values. The simultaneous good predictions of both in-band and interband γ intensities in both bands give a confidence in IBFFM wave functions.

C. Distributions of the parameters characterizing the geometry

We analyze the geometrical properties of the wave functions in the following way. In the case of IBFFM we diagonalize the matrices of the scalar operators $\vec{j}_\pi \cdot \vec{R}$, $\vec{j}_\nu \cdot \vec{R}$, $\vec{j}_\pi \cdot \vec{j}_\nu$, and $\sigma = (\vec{j}_\pi \times \vec{j}_\nu) \cdot \vec{R} = i\sqrt{6}[(j_\pi \otimes j_\nu)_1 \otimes R]_0$, introduced in Ref. [8], where $\vec{j}_\pi, \vec{j}_\nu, \vec{R}$ are the operators of proton, neutron, and core angular momentum, respectively. To the eigenvectors of these operators we assign the following quantities, where $\langle operator \rangle$ denotes the expectation value with the eigenfunction of the operator in the numerator:

$$\cos\psi(j_\pi R) = \frac{\langle \vec{j}_\pi \cdot \vec{R} \rangle}{\sqrt{\langle j_\pi^2 \rangle \langle R^2 \rangle}}, \tag{6}$$

$$\cos\xi(j_\nu R) = \frac{\langle \vec{j}_\nu \cdot \vec{R} \rangle}{\sqrt{\langle j_\nu^2 \rangle \langle R^2 \rangle}}, \tag{7}$$

$$\cos\zeta(j_\pi j_\nu) = \frac{\langle \vec{j}_\pi \cdot \vec{j}_\nu \rangle}{\sqrt{\langle j_\pi^2 \rangle \langle j_\nu^2 \rangle}}, \tag{8}$$

$$\tilde{\sigma} = \frac{\langle i\sqrt{6}[(j_\pi \otimes j_\nu)_1 \otimes R]_0 \rangle}{\sqrt{\langle j_\pi^2 \rangle \langle j_\nu^2 \rangle \langle R^2 \rangle}}, \tag{9}$$

which represent relative angles between proton, neutron, and core angular momentum and the normalized orientation parameter $\tilde{\sigma}$. It is noted that in our case $\tilde{\sigma}$ is somewhat differently normalized than in Ref. [8], where $\sqrt{\langle j_\pi^2 \rangle}$ and $\sqrt{\langle j_\nu^2 \rangle}$ are replaced by $\sqrt{j(j+1)}$.

Projecting the ^{134}Pr IBFFM wave functions onto the four sets of eigenvectors, the distributions of relative angles among proton, neutron, and core angular momentum and of the orientation parameter σ are obtained for ^{134}Pr states calculated in the IBFFM. In Figs. 8–13 the distributions are denoted by Σ. Considering the distributions of the eigenvalues of the geometric operators gives a more detailed picture than only the expectation values studied in Ref. [8].

In the case of the TQPTR, we studied only the orientation parameter σ. Because we use a TQPTR code that is formulated in the body fixed frame, it is more convenient to diagonalize $\sigma = (\vec{j}_\pi \times \vec{j}_\nu) \cdot \vec{J} = i\sqrt{6}[(j_\pi \otimes j_\nu)_1 \otimes J]_0$. It can be shown that the identity $(\vec{j}_\pi \times \vec{j}_\nu) \cdot \vec{J} = (\vec{j}_\pi \times \vec{j}_\nu) \cdot (\vec{R} + \vec{j}_\pi + \vec{j}_\nu) = (\vec{j}_\pi \times \vec{j}_\nu) \cdot \vec{R}$, which is obvious for classical vectors, holds also for the angular momentum operators, i.e., σ is the same orientation operator. The two lowest eigenstates of the TQPTR model are projected on the eigenstates of σ. For simplicity, we consider the special case $\gamma = 30^\circ$, $j_\pi = j_\nu = 11/2$, and irrotational flow ratios $\mathcal{J}_s/\mathcal{J}_l = 1$ and $\mathcal{J}_i/\mathcal{J}_l = 4$, which has also been studied in Ref. [8]. In contrast to the latter, we use a smaller quadrupole coupling strength, which corresponds to the microscopically calculated deformation of $\beta \approx 0.2$, and calculate the distribution eigenvalues of σ instead of its expectation value only. The results are shown in Figs. 8–9,

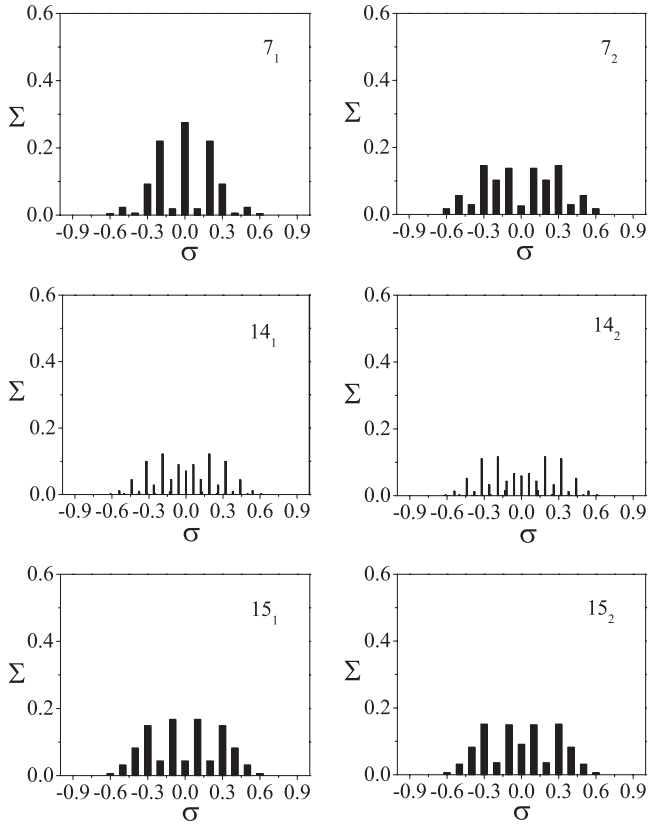

FIG. 8. Distributions of the orientation parameter σ calculated by TQPTR. For the 14^+ states a finer binning (0.01 instead of 0.1) is used to display details of the distribution.

where we normalize the orientation parameter to $\tilde{\sigma} = \sigma/(j(j+1)\sqrt{I(I+1)}$ for practical reasons.

For the case IBFFM, we also study the distribution of the deformation parameters. In IBM the $E2$ boson transition

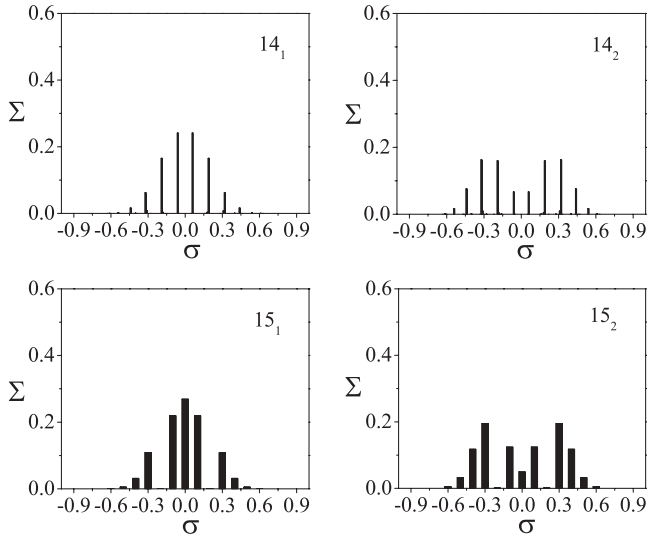

FIG. 9. Distributions of the orientation parameter σ calculated by TQPTR assuming axial shape. For the 14^+ states a finer binning (0.01 instead of 0.1) is used to display details of the distribution.

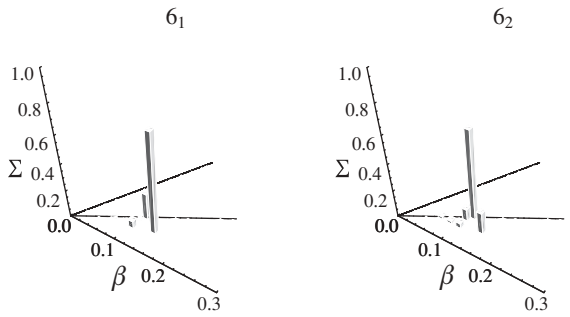

FIG. 10. Distribution of the deformation parameters β and γ for the ground-state band 6_1^+ and γ-band 6_2^+ state in the core ^{134}Ce nucleus. The axes in the β-γ plane have $\gamma = 0^\circ$ and $\gamma = 60^\circ$, whereas the middle line in the β-γ plane marks $\gamma = 30^\circ$.

operator is

$$Q = e_b Q^{\rm IBM}, \tag{10}$$

where the boson charge e_b and $e^{\rm vib}$ used in these calculations are related through:

$$e_b = \frac{3}{4\pi} e R^2 e^{\rm vib}, \tag{11}$$

and $Q^{\rm IBM}$ is the IBM quadrupole operator.

Deformation parameters β and γ can be defined through [56]:

$$\beta^2 = \frac{\sqrt{5}(e^{\rm vib})^2}{Z^2} \langle [Q^{\rm IBM} \otimes Q^{\rm IBM}]_0 \rangle, \tag{12}$$

where Z is the number of protons,

$$\cos 3\gamma = (-)\sqrt{\frac{7}{2\sqrt{5}}} \frac{\langle (Q^{\rm IBM} \otimes [Q^{\rm IBM} \otimes Q^{\rm IBM}]_2)_0 \rangle}{\langle [Q^{\rm IBM} \otimes Q^{\rm IBM}]_0 \rangle^{3/2}}. \tag{13}$$

Again, the operators $[Q^{\rm IBM} \otimes Q^{\rm IBM}]_0$ and $(Q^{\rm IBM} \otimes [Q^{\rm IBM} \otimes Q^{\rm IBM}]_2)_0$ have been diagonalized and the ^{134}Pr IBFFM wave functions projected onto the eigenvectors with assigned β and γ. As both operators are simultaneously diagonal in the same basis (that is not the case with operators associated with relative angles and the orientation parameter), an one-to-one correspondence between β and γ can be established, but having in mind that the distribution in γ is the distribution of the expected effective γ's. The deformation parameter β (12) depends on the choice of $e^{\rm vib}$ (adjusted to the $E2$ transition data) and therefore the β vs. γ distributions can be scaled in the β direction.

D. Orientation parameter in TQPTR model

In Figs. 8–9 we show the distributions of the orientation parameter σ for different excited states calculated by the TQPTR model. In Fig. 9 we report the same distributions assuming axial symmetry.

We compare such idealized case with the experimental results. Bands 1 and 2 are well separated at $I = 7$. They approach each other and cross with a very small interaction near $I = 15$. This has been interpreted as a transition from a chiral vibration to onset of stable chirality [2,18], which is found in the microscopic TAC calculations [2]. The distributions of the orientation parameter support this picture. For $I = 7$, Band 1 shows a maximum for $\sigma = 0$, as expected for the oscillator ground state. Band 2 has a minimum at zero as expected for the first excited state. For $I = 14, 15$, the two bands have similar distributions. Compared with $I = 7$, the large values of σ, i.e., components with large chirality become more probable in Band 1, whereas the distribution of Band 2 does not change dramatically. This is consistent with an earlier change of slope of the function $J(\omega)$ in Band 1 than in Band 2, which was suggested in Ref. [1] (cf. Fig. 4 there) as a signal for onset of chirality. As seen in Fig. 8, the left-handed and right-handed sectors are not well separated. This means chirality materializes only in a dynamical way, namely as a very slow anharmonic vibration. As mentioned we define it as dynamic chirality. The main reason is that the proton and neutron hole are not rigidly bound to the triaxial core, because the deformation is not very large. They execute substantial fluctuations about the respective directions of the short and long axes. The comparison of the TQPTR calculations for axial shape shown in Fig. 9, for which the expectation values $\langle \vec{j}_\pi \rangle$, $\langle \vec{j}_\nu \rangle$, and $\langle \vec{R} \rangle$ are in a plane, with the case of maximal triaxiality, reported in Fig. 8, for which the three vector are no longer in a plane and attain chirality, reflects the prominent role of the fluctuations of the orientation of $\vec{j}_\pi$ and $\vec{j}_\nu$. Considering the lowest state, for $\gamma = 0$, the axial potential does not confine the direction of $\vec{j}_\pi$ in the plane perpendicular to the long axis. The Coriolis force tries to arrange the three vectors in one plane, but there are substantial zero-point fluctuations out of plane, which results in the σ distribution shown in the left panel of Fig. 9. For $\gamma = 30^\circ$, the triaxial potential tries to align $\vec{j}_\pi$ with the short axis, but there are zero-point fluctuations around this direction. The collective angular momentum $\vec{R}$ develops a substantial component along the intermediate axis, which makes the σ distribution noticeably wider. The mean value of σ on one side is about twice as large as for $\gamma = 0$. This means that the solution has attained a chiral character. In the case of the second state, the fluctuations are stronger for both $\gamma = 0$ and $\gamma = 30^\circ$. This is expected for an excited state, which must have more nodes than the ground state. In fact the fluctuations become so prominent that the σ distributions look similar and the mean values of σ are about the same. The discussion shows that the relatively small length of the vectors $\vec{j}_\pi$ and $\vec{j}_\nu$ results in large directional fluctuations, on top of which a dynamical type of chirality develops around $I = 15$. Comparing the results in Figs. 8 and 9, which were done with a finer binning, shows that in the axial case one has fewer lines than in the triaxial case. The quantal coupling of the three types of angular momenta involves substantial fluctuations in their direction, which generates the lines at large $|\sigma|$ for the axial case. In the triaxial case, the presence of many small lines reflects the built up of collective type of chirality on top of the large-$|\sigma|$ lines due to the angular momentum coupling.

E. Analysis of the structure of the IBFFM states

The wave functions of the Bands 1 and 2 show that in the IBFFM picture Band 1 is basically built on the ground-state band of the even-even core. With increasing angular

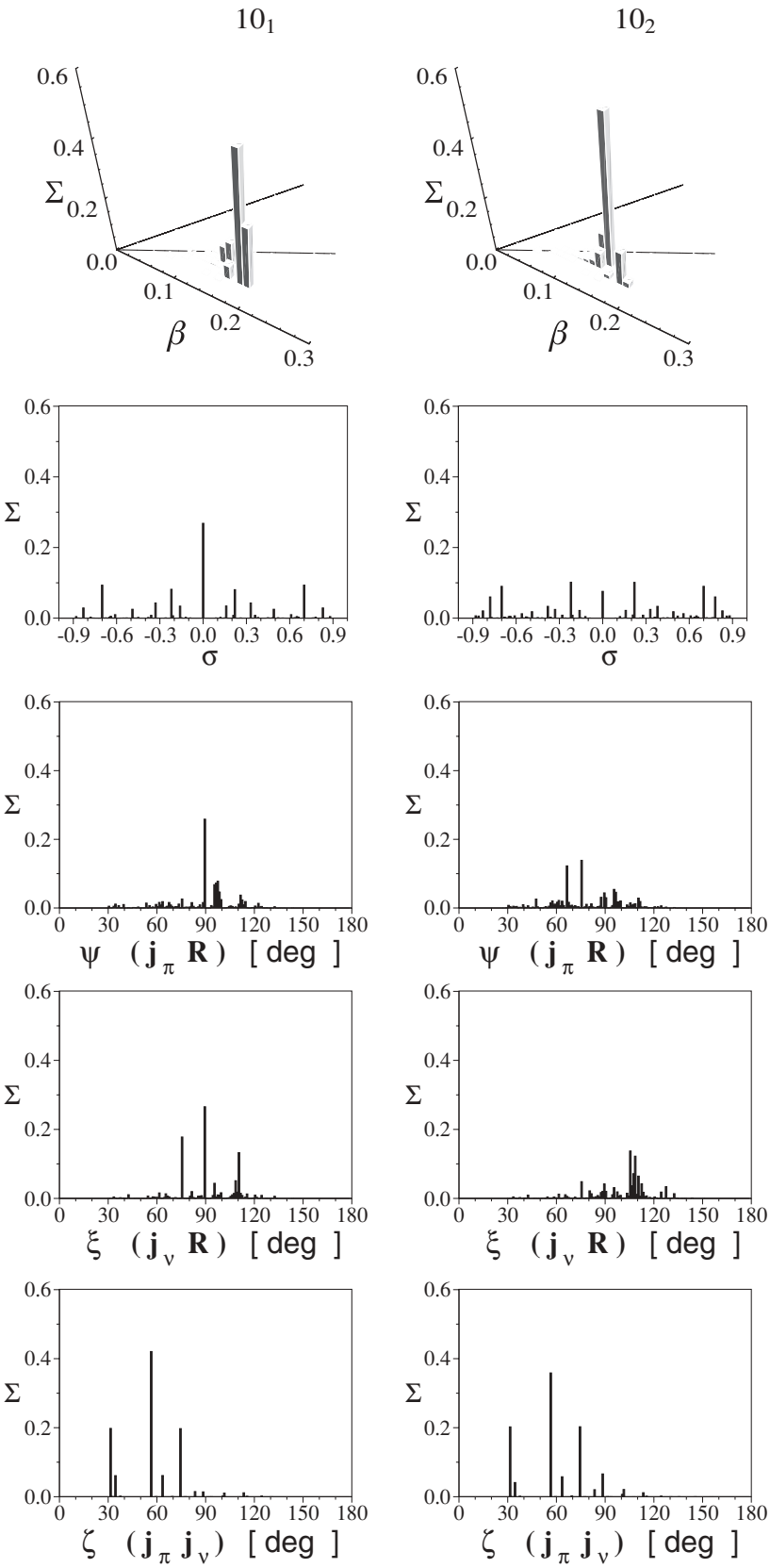

FIG. 11. Distributions of the parameters characterizing the 10_1^+ and 10_2^+ states in ^{134}Pr. The upper panels present the deformation parameters β and γ and orientation parameter σ. The axes in the β-γ plane have $\gamma = 0^\circ$ and $\gamma = 60^\circ$, whereas the middle line in the β-γ plane marks $\gamma = 30^\circ$. The lower panels present the angles $\psi(j_\pi R)$, $\xi(j_\nu R)$, and $\zeta(j_\pi j_\nu)$.

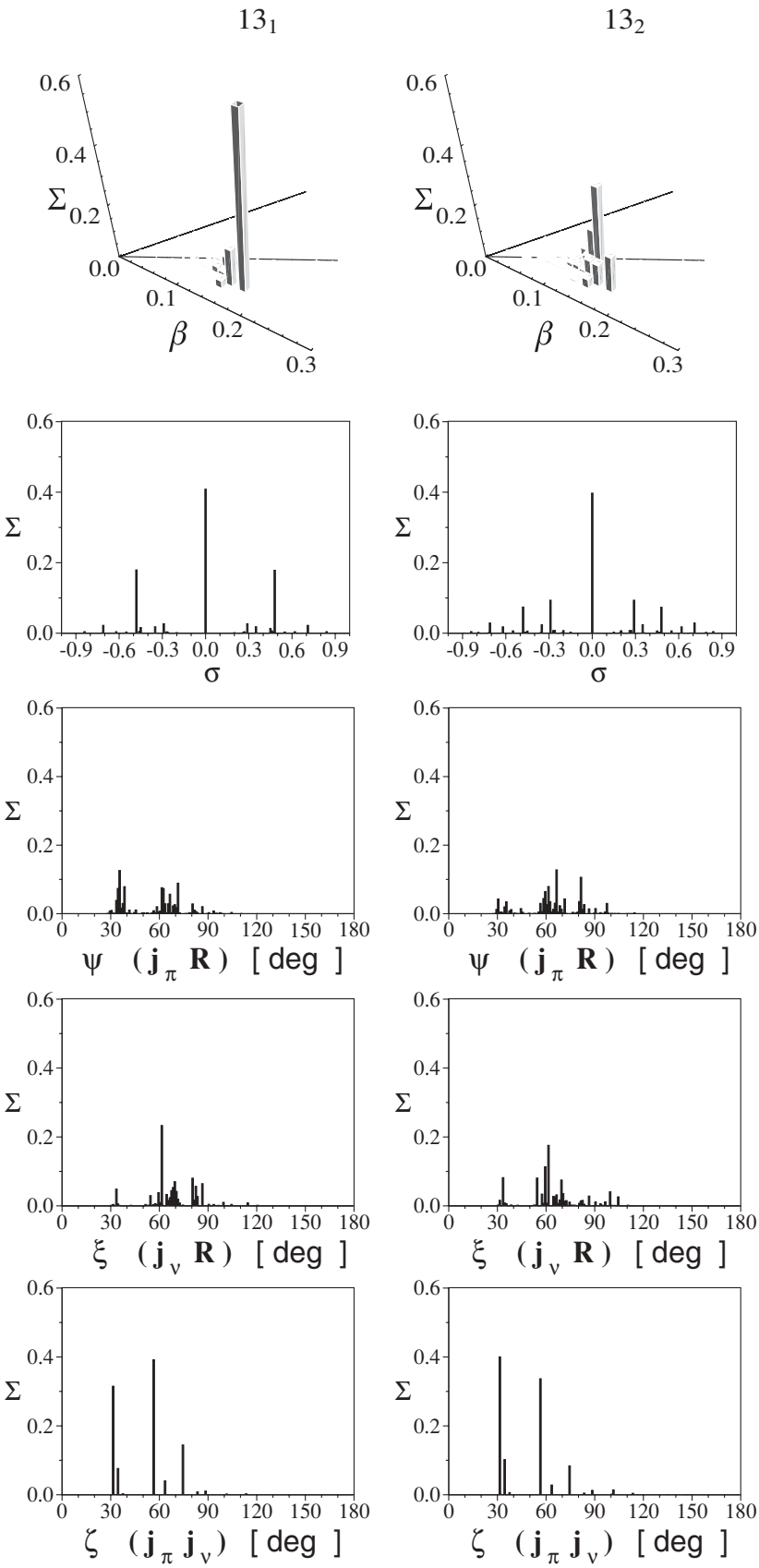

FIG. 12. Distributions of the parameters characterizing the 13_1^+ and 13_2^+ states in ^{134}Pr. The upper panels present the deformation parameters β and γ and orientation parameter σ. The axes in the β-γ plane have $\gamma = 0^\circ$ and $\gamma = 60^\circ$, whereas the middle line in the β-γ plane marks $\gamma = 30^\circ$. The lower panels present the angles $\psi(j_\pi R)$, $\xi(j_\nu R)$, and $\zeta(j_\pi j_\nu)$.

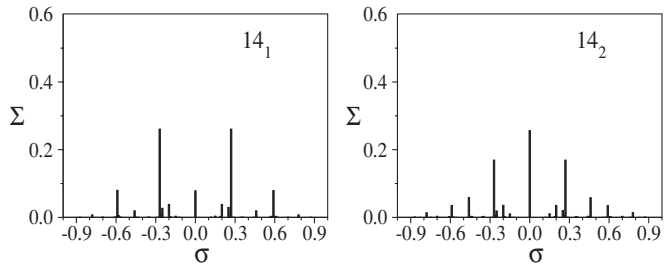

FIG. 13. Distributions of the orientation parameter σ for the 14_1^+ and 14_2^+ states in ^{134}Pr calculated by IBFFM.

momentum the admixture of the γ band of the core becomes more pronounced. The wave functions in Band 2 contain a large component of γ band and, with increasing angular momentum, of higher-lying collective structures of the core.

The distributions of components of wave functions in the core ^{134}Ce nucleus for states of the γ band are almost centered at $\gamma = 30^\circ$, whereas in the ground-state band they are shifted to smaller values. Higher bands are characterized by $\gamma \approx 30^\circ$ dominant components, too. The admixture of the γ band of the core in ^{134}Pr Band 1 and dominance of the γ band in Band 2 indicate the presence of triaxiality, which is the prerequisite for a chiral interpretation of these bands. For example, Fig. 10 presents the distribution of the deformation parameters β-γ for the ground-state band 6_1^+ and γ-band 6_2^+ states in the core ^{134}Ce nucleus. In Fig. 10 (as well as in other figures displaying β-γ distributions) the axes in the β-γ plane have $\gamma = 0^\circ$ and $\gamma = 60^\circ$, whereas the middle line in the β-γ plane marks $\gamma = 30^\circ$.

The β-γ distribution in Band 1 of ^{134}Pr is very similar to that of the ground-state band of the core, but the maximum is shifted to smaller values. The boson-fermion interaction drags the soft triaxial core toward the prolate shape. This dynamical effect not only compensates but also overcomes the opposite tendency (toward $\gamma = 30^\circ$) of contributions from large γ-band components in the wave functions. The fluctuations of the parameter γ in Band 1 increase with angular momentum. In Band 2 the fluctuations of the parameter γ are more pronounced. Components with lower γ are smaller. The dominant components lie between 20° and 25°. For states of higher angular momenta in Band 2 the fluctuations of γ are very large. The β distribution of Band 1 has its maximum at larger deformations than one of Band 2. At higher angular momenta, this difference becomes very pronounced. In both bands the distribution is gradually shifted toward smaller values of β with increasing angular momentum. This tendency is stronger in Band 2. In addition, the fluctuations of β in Band 2 become very large with increasing angular momentum. Even very small deformations appear in the distribution. The different deformations indicate that the two bands cannot be even and odd superpositions of well-separated left-handed and right-handed configurations. In such a case of static chirality, the boson-fermion coupling would be identical for both bands. The different σ distributions show that this is not the case, which is consistent with a strong $\sigma = 0$ (achiral) component. Nevertheless, the following analysis of relative angles shown in Figs. 11–13 among the proton, neutron, and core angular momenta points to presence of dynamical chirality.

The distributions $\zeta(j_\pi j_\nu)$ of the angle between $\vec{j}_\pi$ and $\vec{j}_\nu$ are similar for both Bands 1 and 2, corresponding to an average angle of about 60° for $I = 10$. The distributions for $I = 13$ are much the same corresponding to a somewhat smaller average angle, which is a consequence of the Coriolis force. The similarity of the distributions indicates that Band 1 and 2 differ mainly by their composition in the core angular momentum $\vec{R}$. For the state 10_1 the distributions $\psi(j_\pi R)$ and $\xi(j_\nu R)$ have a wide maximum not far from 90°. For the state 10_2, the distributions are also centered not far from 90° but scattered across almost the whole range of angles. The wide distributions are expected because the core angular momentum R is small and dominated by fluctuations, which are stronger in the excited state. They indicate a weak fluctuation dominated chirality. For the states 13_1 and 13_2, the distributions $\psi(j_\pi R)$ and $\xi(j_\nu R)$ are somewhat more narrow and the center is moved to the region around 60°. The narrowing is a consequence of the increase of R and the shift of the center is caused by the Coriolis force. The distributions of the orientation parameter σ presented in Figs. 11–13 show substantial chiral components. However, all have a strong $\sigma = 0$ component, which indicates that chirality materializes only as large-amplitude vibrations. To see the influence of the γ degree of freedom, we calculated the same distributions for the case of the SU(3) symmetry, i.e., for axial shape. The SU(3) distributions have typically only few strong lines, which correspond to the few strongest lines in Figs. 11–13. As for the case of TQPTR, these lines represent the quantal coupling of the three kinds of angular momenta, which involves substantial values of $|\sigma|$. The many additional small lines in the realistic case are consistent with the presence of a dynamical chirality on top of these quantum fluctuations. The SU(3) type of lines are more prominent in the realistic IBFFM spectrum than the axial lines in the triaxial spectrum in the case of TQPTR. This is expected, because the effective triaxialty in the IBFFM case is substantially less than for TQPTR, which has $\gamma = 30^\circ$. In addition, the fluctuations of γ in the IBFFM admix near-axial components.

For the lowest angular momenta, the maxima of both angles $\psi(j_\pi R)$ and $\xi(j_\nu R)$ are sizable larger than 90°. This situation is typical for vibrational nuclei where fermions are coupled to the core by strong boson-fermion interactions, indicating that for the lowest angular momenta of both bands the composition of the core angular momentum is complex. Its major part in the IBFFM picture is not of rotational origin.

For angular momenta $I \geqslant 11$ the picture changes. With increasing angular momentum, $\zeta(j_\pi j_\nu)$ in both bands shifts very slowly toward smaller angles, leaving enough components that are favorable for the chiral structure. The behavior of $\xi(j_\nu R)$ and $\psi(j_\pi R)$ is similar, with the difference that $\psi(j_\pi R)$ more rapidly increases its tendency toward small angles. The distribution of the orientation parameter shows components with sizable σ. The immediate conclusion turns out to be misleading. Inspecting the distributions in a similar axial prolate SU(3) case, the figures are not very different. Nevertheless, some differences are present. Components with the geometry favorable for chirality are larger in the ^{134}Pr case than in the axial prolate SU(3) case, but the effect is in average smaller than 20%. The chiral condition of equal distributions

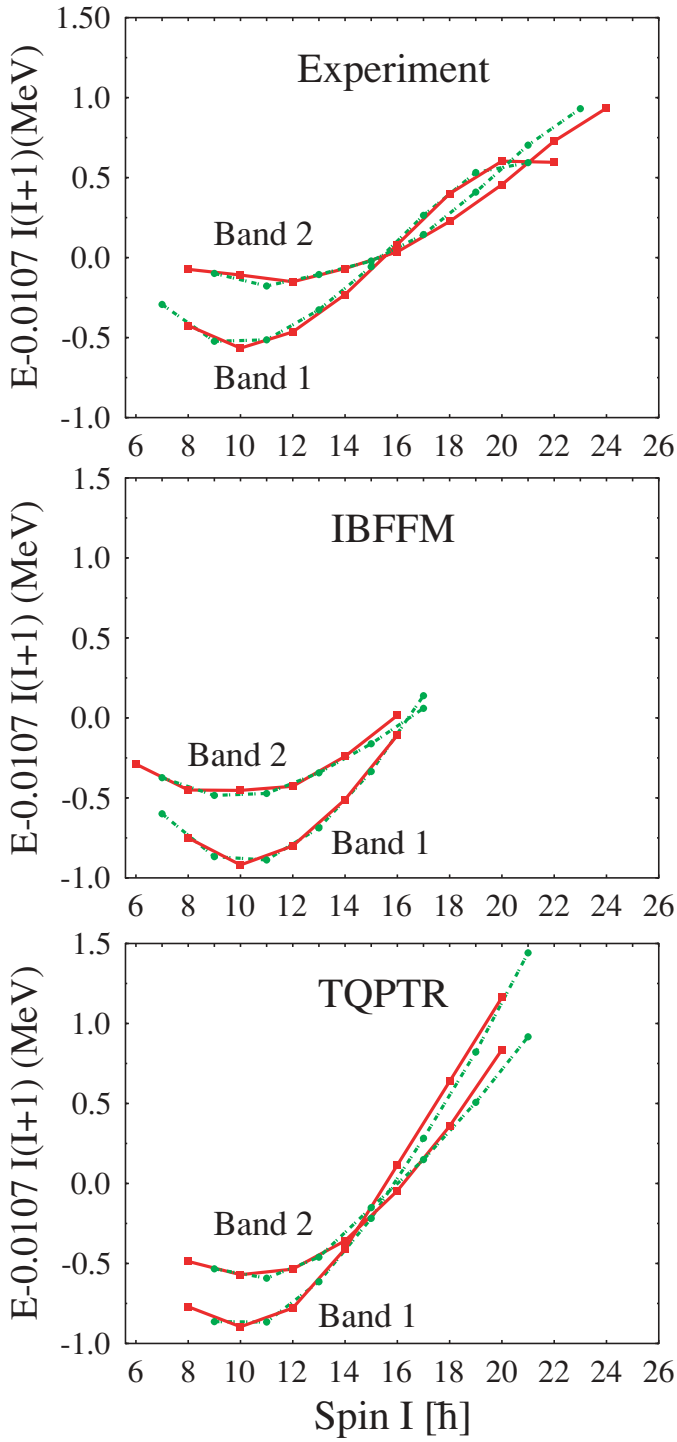

FIG. 14. (Color online) The excitation energies in both chiral candidate bands are plotted relative to a rigid rotor. The value of the normalization parameter is choosen 0.0107 as in the work [21] to obtain a smooth behavior of the curves. In all panels curves for even-even spin difference $\Delta I = 2$ are presented by the full line, whereas for the odd-odd spin difference $\Delta I = 2$ are shown with a dashed line. In such a way relative energies of the partner bands calculated in the IBFFM and TQPTR are compared to the experimental ones.

in states of the same angular momentum in both bands is better fulfilled in ^{134}Pr, but it is far from being reached. In Fig. 12 typical distributions are presented for 13^+_1 and 13^+_2 states. For $I \geqslant 11$ all odd angular momentum states of Bands 1 and 2 have σ distributions similar to those presented in Fig. 12, whereas even angular momentum states have σ distributions similar to those presented in Fig. 13.

F. Comparison with the experimental results

As is seen in Fig. 14, the TQPTR calculations based on the microscopic moments of inertia reproduce very well the relative energies of the partner bands, in particular the sharp crossing of the bands at $I = 15$. The remarkable observation is that the interaction between the two $I = 15$ states must be less than 20 keV, whereas there are strong interband transitions

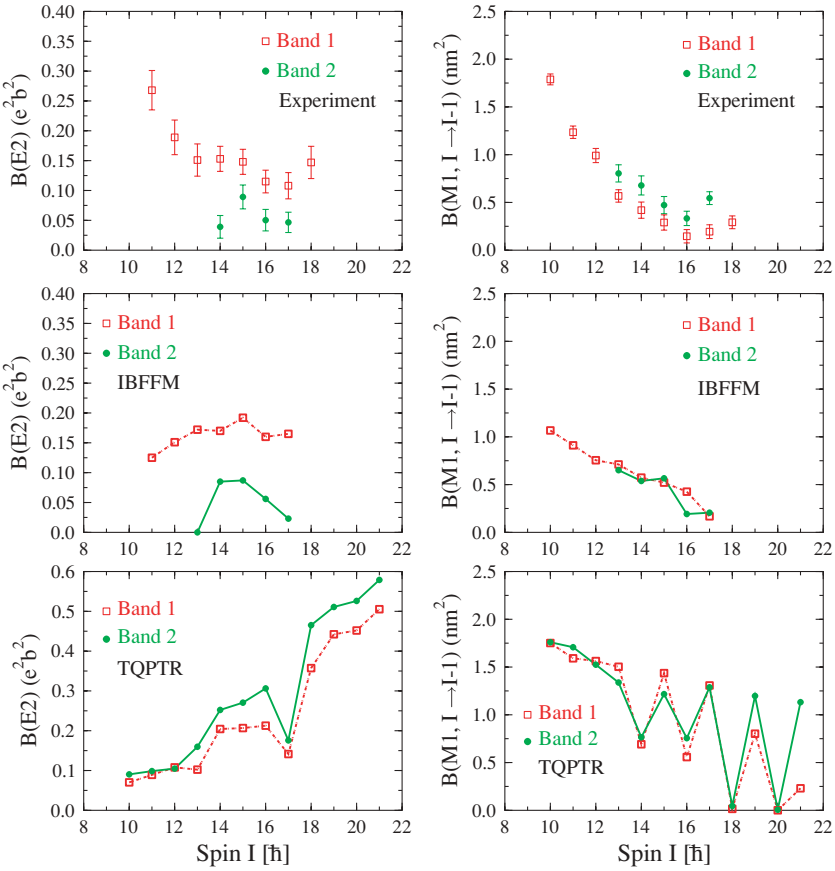

FIG. 15. (Color online) Experimentally determined and theoretically calculated values for in-band $B(E2)$ and $B(M1)$ values in ^{134}Pr. In the upper panels experimental $B(E2)$ and $B(M1)$ values in Band 1 and Band 2 are presented. In the middle panel the predictions of the TQPTR are presented. In the panel on the bottom the calculations of the IBFFM are shown. The spin assignments for band members above spin 15 in TQPTR calculations have been arranged in a different way in respect to the assignments in Ref. [20]. See also the text.

born out by the TQPTR model. This demonstrates that the small interaction strength need not to be the consequence of different shapes of the two bands, as claimed in Ref. [21]. The energy distance between the two bands calculated by means of the IBFFM is larger than in experiment. The two bands approach each other; however, they do not cross near $I = 15$. We find that the IBFFM cannot generate such crossing within a reasonable range of its parameter space.

The change of curvature of the experimental Band 1 in Fig. 14 signals the rotational alignment of two quasiparticles (see the alignment plot in Ref. [21]). Hence above $I = 16$ Band 1 has no longer the two quasiparticle character assumed both in the TQPTR and IBFFM calculations. A comparison between the experimental and calculated in-band transition rates in Band 1 as well as between experimental and calculated interband transition rates show large disagreements.

Figures 15, 16, and 17 compare the experimental with the calculated electromagnetic transition probabilities.[1] As already pointed out in the preceding publication [20], the measured electromagnetic transition probabilities deviate substantially from the TQPTR calculations. The calculated $B(M1)$ values show a pronounced staggering behavior, the reason of which was discussed for a special case in Ref. [57]: The large reduced transition probabilities alternate between intra- and interband transitions. No such alternation is seen in the present data. Rather, the in-band probabilities are large as compared with the interband values. The absence of the alternation, which makes every second in-band transition weak and every second interband transition strong, is the most striking discrepancy. The sums of the strengths of the in-band and interband transitions from a level are comparable, although the decrease with spin is somewhat weaker in the TQPTR calculation than in experiment. The observed $B(E2)$ values for inband transitions are about a factor of 2 larger in Band 1 than Band 2, whereas TQPTR gives similar $B(E2)$ values for both bands. The TQPTR values of $B(E2, 16_2 \rightarrow 14_1)$ and $B(E2, 14_2 \rightarrow 12_1)$ come close to those of the experiment, whereas the upper limit for $B(E2, 13_2 \rightarrow 11_1)$ lies below the TQPTR value.

In the case of IBFFM, the calculated in-band $B(E2)$ values for Band 1 (Fig. 15) are in good agreement with the measured values [20]. For an O(6) γ-unstable nucleus the $B(E2)$ values would be very small, even vanishing, for low angular momenta. The fluctuations of γ and the shift of γ_{eff} toward smaller angles admix large near-axial shapes. The admixture of near axial shapes in the IBFFM increases the $B(E2)$ values at a low angular momentum. However, IBFFM cannot reproduce the large values of $B(E2)$ for the lowest states in Band 1. This is a

[1]Figure 15 is slightly changed as compared to Fig. 3 of Ref. [20]. For TQPTR, we exchanged the assignment of the $I = 15$ states to Bands 1 and 2, because this assignment agrees better with the observed systematics of the transition probabilities. The two 14^+ states are nearly degenerate and mixed as a result of their weak interaction; the assignment to the two bands is to some extent ambiguous. We arranged them such that the intraband $E2$ transitions are larger than the interband transitions. This results in an exchange comparable to that of Ref. [20].

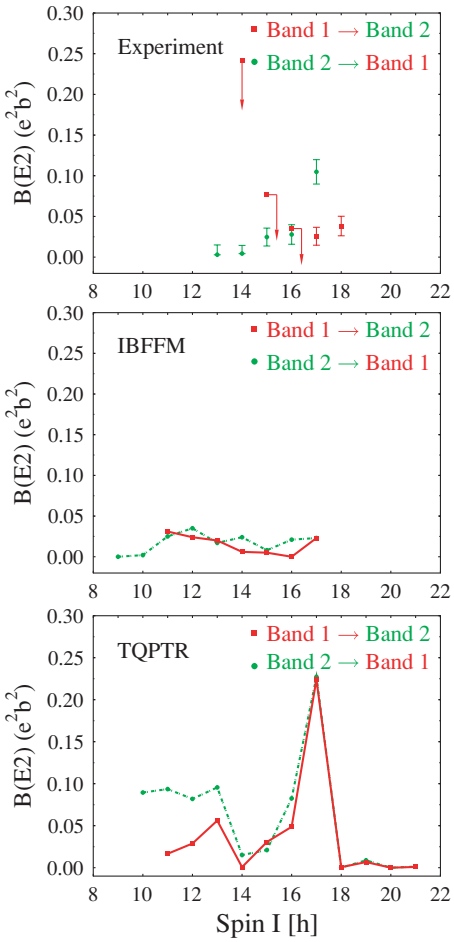

FIG. 16. (Color online) Experimentally determined and theoretically calculated interband $B(E2)$ values in ^{134}Pr. In the upper panel experimental $B(E2)$ values from Band 1 to Band 2 and from Band 2 to Band 1 are presented. With arrows are presented limits for the $B(E2)$ values for the states with $I^{\pi} = 13^{+}$ to 16^{+}. In the middle panel the predictions of the IBFFM are presented. In the panel on the bottom the predictions of the TQPTR are presented. See also text.

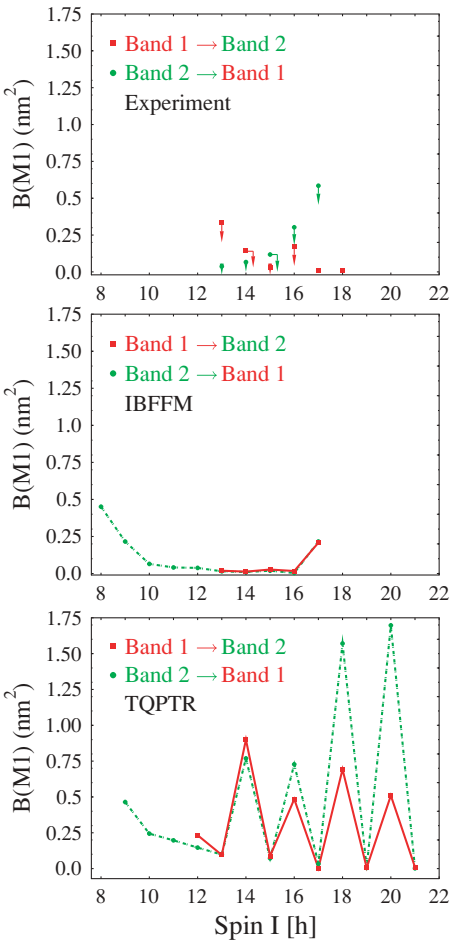

FIG. 17. (Color online) Experimentally determined limits and theoretically calculated values for interband $B(M1)$ values in ^{134}Pr. In the upper panel experimental $B(M1)$ limits from Band 1 to Band 2 and from Band 2 to Band 1 are presented. In the middle panel the predictions of the IBFFM are presented. In the panel on the bottom the calculations of the TQPTR are shown. See also text.

consequence of a complex structure of the IBFFM core angular momentum at low angular momentum that reassembles more a vibrational than a rotational character. In the case of an O(6) γ-unstable as well as for an axial SU(3) prolate nucleus, the $B(E2)$ values in Band 1 would increase with increasing angular momentum. This tendency would be stopped and reversed only by the effects of the finite boson space at very high angular momentum. In the present IBFFM calculation the $B(E2)$ values remain almost constant with a tendency of decreasing already at $I = 16$. This is a consequence of the gradual shift of β toward smaller values with increasing angular momentum and is in perfect accordance with the experiment.

For $I = 14$–17 experimental and IBFFM inband $B(E2)$ values for Band 2 are in almost perfect agreement. For these, as well as for other angular momenta, the IBFFM in-band $B(E2)$ values are sizably and systematically smaller for Band 2 than for Band 1, as a consequence of smaller β in Band 2. The drop of $B(E2)$ to 0.0002 e^2b^2 for $I = 13$ reflects the very pronounced γ softness and the dominant components with γ between 20° and 25° in the wave functions of the states of Band 2, i.e., reflects a structure rather similar to O(6). If the admixture of more axial components is stronger, this minimum disappears.

As seen in Fig. 15, the calculated and experimental $B(M1)$ values are nearly the same in both bands [20]. The absence of the staggering in the IBFFM is due to fluctuations of the shape with contributions from near axial shapes that wash out the staggering at high spin. Therefore, the experimental difference between the $B(E2)$ values in Bands 1 and 2 and the absence of the pronounced staggering of the $B(M1)$ values, indicate that the coupling due to shape fluctuations plays a central role in the structure of the twin bands in ^{134}Pr.

The calculated interband decay pattern of Band 1 agrees well with the observed one. Comparison of the experimentally derived and theoretically determined $B(E2)$ values are shown in Fig. 16. The predicted $\Delta I = 1 B(M1)$ values for transitions from Band 1 into Band 2 states are of the order of 0.02 μ_N^2

(cf. Fig. 17), except for a rather strong $17_1^+ \rightarrow 16_2^+$ transition that was not observed.

The $E2$ transitions from Band 2 into Band 1 states are well reproduced by the model. In the IBFFM calculation $B(E2)$ values in the range 0.008–0.035 e^2b^2 are predicted, except for the $10_2^+ \rightarrow 8_1^+$ and $9_2^+ \rightarrow 7_1^+$ transitions where very small $B(E2)$ values 0.002 and 0.0002 e^2b^2 are obtained. The theoretical values are inside the experimental error bars. The only exception is a rather big experimental $B(E2)$ value for the $17_2^+ \rightarrow 15_1^+$ transition that the present calculation is not reproducing. A very good agreement is found between theory and experiment for $\Delta I = 1$ interband $2 \rightarrow 1$ transitions (Fig. 7). The $B(M1)$ values sharply decrease from 0.451 μ_N^2 for $8_2^+ \rightarrow 7_1^+$ to 0.065 μ_N^2 for $10_2^+ \rightarrow 9_1^+$ transition. The trend of decreasing $B(M1)$ values smoothly continues to 0.010 μ_N^2 for $14_2^+ \rightarrow 13_1^+$. The experimental branching ratios indicate that for the next three states of Band 2 the interband $B(M1)$ values should increase. Indeed, the calculated $17_2^+ \rightarrow 16_1^+ B(M1) = 0.216\ \mu_N^2$ fits in this trend, but the calculated weak $16_2^+ \rightarrow 15_1^+$ transition does not. The $\Delta I = 0$ transitions are forbidden. All calculated reduced transition probabilities are smaller than 0.004 μ_N^2 with an even smaller $E2$ component, and for many transitions the forbiddeness is almost exact.

The IBFFM calculation clearly predicts two states with angular momenta 7^+ and 6^+ below the state 8_2^+, that on the basis of their wave functions and $B(M1)$ values are members of Band 2 (Fig. 7). Due to small transition energies for in-band transitions, these two states are not likely to be observed in experiment. The IBFFM prediction is that in the decay pattern of the 8_2^+ state, the 7_2^+ is populated by a γ ray with an intensity of only 3% of the that of the already weak $8_2^+ \rightarrow 7_1^+$ transition. The $7_2^+ \rightarrow 6_2^+$ γ ray would have an intensity of 5% of that of the dominant $7_2^+ \rightarrow 8_1^+$ transition. Finally, the 6_2^+ band head would decay exclusively to the 7_1^+ band head of Band 1.

VI. CONCLUSIONS

Lifetimes in the two chiral candidates bands in ^{134}Pr were measured by means of the recoil distance Doppler-shift and Doppler-shift attenuation method. The branching ratios and electric or magnetic character of the transitions were also investigated. We have determined the electromagnetic transition probabilities for the two bands in ^{134}Pr, which have been suggested to be chiral partners. To judge to what extend this interpretation is supported by our measurements we applied two theoretical models, TQPTR and IBFFM. Both models couple a $h_{11/2}$ particle-like quasiproton and a $h_{11/2}$ hole-like quasineutron to the even-even core. In the case of the TQPTR the core is a rigid triaxial rotor, the deformation of which and its moments of inertia were calculated by means of the TAC mean field theory. The TQPTR takes into account only the orientation of the angular momenta of the particle, of the hole, and of the core. The TQPTR describes very well the energies of the two bands, in particular the conspicuous sharp crossing between the two bands. However, there are two discrepancies concerning the electromagnetic transition probabilities: (i) the calculated inband $B(E2)$ values are about the same for both bands, whereas the measured ones differ by a factor of 2. (ii) The calculations give strong $B(M1)$ [and unstretched $B(E2)$] values that alternate with spin between in-band and interband transitions, whereas the experimental inband values are large and the interband values are small.

The IBFFM core has the deformation parameters as additional degrees of freedom, which are described by the IBM. Because the standard boson IBM-1 Hamiltonian with one- and two-body interactions encompasses only the case of γ instability, we have included three-body boson terms in the Hamiltonian that induce triaxiality. Adjusting the parameters to the even-even neighbors, the potential energy surface has a minimum around $\gamma = 20^\circ$, which is very shallow in the γ direction and also rather broad in the β direction. The γ-decay properties of levels in ^{134}Pr, calculated in this framework, are in excellent agreement with experimental data. However, the calculated energy splitting between the two bands is too large. The observed crossing between the two bands at $I = 15$ cannot be reproduced.

We analyzed the structure of the wave functions by calculating distributions of the mutual angles between the proton, neutron, and core angular momenta, their triple product (orientation parameter), and the deformation parameters. At low spin, the TQPTR distributions have the character of a zero and one-phonon state of a chiral vibration. At larger spin, where the bands cross, the two distribution become very similar, as expected for static chirality. However, the substantial presence of achiral configurations indicates that the chirality is dynamic, i.e., some slow, strongly anharmonic excursion of the angular momentum vector into the left- and right-handed sectors. The IBFFM distributions show a similar trend, but the transition is not as clearly visible. The presence of configurations with the angular momenta of the proton, neutron and core in the favorable, almost orthogonal geometry, is substantial but far from being dominant. There are large fluctuations of the deformation parameters β and γ around the triaxial equilibrium shape, which enhance the content of achiral configurations in the wave function.

The present study suggests that the existence of the two crossing $\Delta I = 1$ bands with the same parity in ^{134}Pr should be attributed to a weak fluctuation dominated chirality combined with an intrinsic symmetry yet to be revealed.

ACKNOWLEDGMENTS

D.T. express his gratitude to Ivanka Necheva for her outstanding support. This research has been supported by a Marie Curie Fellowship under contract number HPMF-CT-2002-02018, by the European Commission through contract number HPRI-CT-1999-00078, by the BMBF under contract number 06K167, and by the U.S. Department of Energy by the contract numbers DE-FG02-95ER40934 and DE-FG02-96ER40983. D. T. and P. P. are indebted to the National Science Fund at the Bulgarian Ministry of Education and Science for a financial support.

[1] S. Frauendorf and J. Meng, Nucl. Phys. **A617**, 131 (1997).
[2] V. I. Dimitrov, S. Frauendorf, and F. Dönau, Phys. Rev. Lett. **84**, 5732 (2000).
[3] K. Starosta, T. Koike, C. J. Chiara, D. B. Fossan, and D. R. LaFosse, Nucl. Phys. **A682**, 375c (2001).
[4] S. Frauendorf, Rev. Mod. Phys. **73**, 463 (2001).
[5] C. Vaman, D. B. Fossan, T. Koike, K. Starosta, I. Y. Lee, and A. O. Macchiavelli, Phys. Rev. Lett. **92**, 032501 (2004).
[6] J. Timar *et al*., Phys. Lett. **B598**, 178 (2004).
[7] P. Joshi *et al*., Phys. Lett. **B595**, 135 (2004).
[8] K. Starosta, C. J. Chiara, D. B. Fossan, T. Koike, T. T. S. Kuo, D. R. LaFosse, S. G. Rohoziński, Ch. Droste, T. Morek, and J. Srebrny, Phys. Rev. C **65**, 044328 (2002).
[9] S. Zhu *et al*., Phys. Rev. Lett. **91**, 132501 (2003).
[10] G. Rainovski *et al*., Phys. Rev. C **68**, 024318 (2003).
[11] A. A. Hecht *et al*., Phys. Rev. C **68**, 054310 (2003).
[12] E. Grodner *et al*., Phys. Rev. Lett. **97**, 172501 (2006).
[13] D. L. Balabanski *et al*., Phys. Rev. C **70**, 044305 (2004).
[14] J. Peng, J. Meng, and S. Q. Zhang, Phys. Rev. C **68**, 044324 (2003).
[15] P. Olbratowski, J. Dobaczewski, J. Dudek, and W. Plóciennik, Phys. Rev. Lett. **93**, 052501 (2004).
[16] J. Meng, J. Peng, S. Q. Zhang, and S.-G. Zhou, Phys. Rev. C **73**, 037303 (2006).
[17] C. M. Petrache, D. Bazzacco, S. Lunardi, C. Rossi Alvarez, G. de Angelis, M. De Poli, D. Bucurescu, C. A. Ur, P. B. Semmes, and R. Wyss, Nucl. Phys. **A597**, 106 (1996).
[18] K. Starosta *et al*., Phys. Rev. Lett. **86**, 971 (2001).
[19] S. Brant, D. Vretenar, and A. Ventura, Phys. Rev. C **69**, 017304 (2004).
[20] D. Tonev *et al*., Phys. Rev. Lett. **96**, 052501 (2006).
[21] C. M. Petrache, G. B. Hagemann, I. Hamamoto, and K. Starosta, Phys. Rev. Lett. **96**, 112502 (2006).
[22] J. Simpson, Z. Phys. A **358**, 139 (1997).
[23] A. Dewald, S. Harissopulos, and P. von Brentano, Z. Phys. A **334**, 163 (1989).
[24] G. Böhm, A. Dewald, P. Petkov, and P. von Brentano, Nucl. Instrum. Methods Phys. Res. A **329**, 248 (1993).
[25] P. Petkov, D. Tonev, J. Gableske, A. Dewald, T. Klemme, and P. von Brentano, Nucl. Instrum. Methods Phys. Res. A **431**, 208 (1999).
[26] K. Starosta, in *Nuclei at the Limits*, edited by T. L. Khoo and D. Seweryniak, AIP Conf. Proc. No. 764 (AIP, New York, 2005), p. 77.
[27] P. Petkov, A. Dewald, R. Kühn, R. Peusquens, D. Tonev, S. Kasemann, K. O. Zell, P. von Brentano, D. Bazzacco, C. Rossi-Alvarez, G. de Angelis, S. Lunardi, P. Pavan, and D. R. Napoli, Nucl. Phys. **A674**, 357 (2000).
[28] P. Petkov *et al*., Nucl. Phys. **A640**, 293 (1998).
[29] G. Winter, ZfK Rossendorf Report ZfK-497 (1983).
[30] G. Winter, Nucl. Instrum. Methods **214**, 537 (1983).
[31] W. M. Currie, Nucl. Instrum. Methods Phys. Rev. A **73**, 173 (1969).
[32] T. K. Alexander and J. S. Forster, Adv. Nucl. Phys. **10**, 197 (1978).
[33] P. M. Jones, L. Wei, F. A. Beck, P. A. Butler, T. Byrski, G. Duchene, G. de France, F. Hannachi, G. D. Jones, and B. Kharraja, Nucl. Instrum. Methods Phys. Res. A **362**, 556 (1995).
[34] A. Gadea *et al*., *Facing the Next Millennium 1999*, edited by B. Rubio, M. Lozano, and W. Gelletly, AIP Conf. Proc. No. 495 (AIP, New York, 1999), p. 195.
[35] O. Klein and Y. Nishina, Z. Phys. **52**, 853 (1929); Y. Nishina, Z. Phys. **52**, 869 (1929).
[36] M. A. Jones *et al*., Nucl. Phys. **A605**, 133 (1996).
[37] T. Klemme *et al*., Phys. Rev. C **60**, 034301 (1999).
[38] S. P. Roberts, T. Ahn, K. Starosta, T. Koike, C. J. Chiara, and C. Vaman, Phys. Rev. C **67**, 057301 (2003).
[39] I. Ragnarsson and P. Semmes, Hyperfine Interact. **43**, 425 (1988).
[40] V. Paar, in *Capture Gamma-Ray Spectroscopy and Related Topics—1984*, edited by S. Raman, AIP Conf. Proc. No. 125 (AIP, New York, 1985), p. 70; S. Brant, V. Paar, and D. Vretenar, Z. Phys. A **319**, 355 (1984); V. Paar, D. K. Sunko, and D. Vretenar, Z. Phys. A **327**, 291 (1987).
[41] S. Brant and V. Paar, Z. Phys. A **329**, 151 (1988).
[42] F. Iachello and A. Arima, *The Interacting Boson Model* (Cambridge University Press, Cambridge, 1987).
[43] A. Arima and F. Iachello, Phys. Rev. Lett. **35**, 157 (1975); Ann. Phys. (NY) **99**, 233 (1976); **111**, 201 (1978); **123**, 468 (1979).
[44] F. Iachello and O. Scholten, Phys. Rev. Lett. **43**, 679 (1979).
[45] F. Iachello and P. Van Isacker, *The Interacting Boson Fermion Model* (Cambridge University Press, Cambridge, 1991).
[46] G. Catadanil, D. Bucurescu, A. Gizon, and J. Gizon, J. Phys. G **20**, 1051 (1994).
[47] T. Mizusaki and T. Otsuka, Prog. Theor. Phys. Suppl. **125**, 97 (1996).
[48] L. Wilets and M. Jean, Phys. Rev. **102**, 788 (1956).
[49] Y. F. Smirnov, N. A. Smirnova, and P. Van Isacker, Phys. Rev. C **61**, 041302(R) (2000).
[50] T. Otsuka and M. Sugita, Phys. Rev. Lett. **59**, 1541 (1987).
[51] M. Sugita, T. Otsuka, and A. Gelberg, Nucl. Phys. **A493**, 350 (1989).
[52] O. Vogel, P. Van Isacker, A. Gelberg, P. von Brentano, and A. Dewald, Phys. Rev. C **53**, 1660 (1996).
[53] R. V. Jolos, P. von Brentano, N. Pietralla, and I. Schneider, Nucl. Phys. **A618**, 126 (1997).
[54] K. Heyde, P. Van Isacker, M. Waroquier, and J. Moreau, Phys. Rev. C **29**, 1420 (1984).
[55] R. F. Casten, P. von Brentano, K. Heyde, P. Van Isacker, and J. Jolie, Nucl. Phys. **A439**, 289 (1985).
[56] V. Werner, N. Pietralla, P. von Brentano, R. F. Casten, and R. V. Jolos, Phys. Rev. C **61**, 021301(R) (2000).
[57] T. Koike, K. Starosta, and I. Hamamoto, Phys. Rev. Lett. **93**, 172502 (2004).